POLITECNICO DI TORINO

Master's Degree in Energy and Nuclear Engineering

Politecnico
di Torino

Master's Degree Thesis

Bayesian optimization of the CHERAB code for the reconstruction of the D-α camera view in ST40 tokamak

Supervisors

Prof. Fabio SUBBA

Ing. Matteo MOSCHENI

Candidate

Raffaele PIERGALLINI

November 2023

Abstract

The next generation of nuclear fusion devices aims to achieve and sustain significantly improved plasma performance compared to existing tokamaks. This requires reliable quantification of plasma properties, power, and particle exhaust during the design phase and diagnosis during operations. Moreover, unprecedented levels of neutron irradiation are expected in pilot plants, which pose operational and servicing challenges. In this context, synthetic diagnostics are valuable tools for the fusion community. They support the interpretation of experimental data, which is inherently challenging, and enable careful diagnostic design and integrated analyses for capturing essential plasma features. The D-α camera, for example, can infer properties of the neutral deuterium distribution in the chamber, making it useful for diagnosing the edge plasma, particularly in detached divertor regimes.

This work, conducted in collaboration with Tokamak Energy Ltd, utilizes the 3D Monte-Carlo inverse ray-tracing software CHERAB to simulate the 2D perspective of a synthetic D-α camera within the ST40 tokamak. The primary objective is to extract valuable neutral parameters from these simulations. To accomplish this, the D-α emission source is created using simplified analytical models for both the core and edge plasma. These models involve numerous free parameters, necessitating their optimization to accurately match experimental results. Due to the inherent characteristics of the Monte-Carlo code, the optimization process necessitates the utilization of a derivative and gradient-free method. Specifically, Bayesian optimization process is employed for this purpose. In the two plasma shots examined, a notable level of qualitative agreement has been observed, although achieving precise quantitative agreement poses a significant challenge due to the inherent three-dimensional nature of the ST40 neutral emission originating from the wall.

Acknowledgements

I would like to express my gratitude to my family, with a special mention of my dad, for their support throughout this journey. Their encouragement and understanding have been my strength.

I extend my sincere thanks to my professor Subba and Matteo, without them this experience would not have been possible. A special thanks also to the Tokamak Energy people that helps me in this journey.

A special thanks also goes to my partner, who has been able to support me at every moment.

Contents

List of Figures

Chapter 1

Introduction

1.1 Nuclear Fusion

Over the last few decades, the world has deal with mounting environmental concerns, necessitating a radical shift away from fossil fuels and towards sustainable energy alternatives. In this context, nuclear fusion emerges as one of the most promising technologies for achieving a continuous and sustainable energy source. Specifically, when integrated into a well-balanced energy mix, it has the potential to meet the 'base load' requirement, which denotes the minimum power supply essential for the grid. This capability is challenging for renewable energy sources due to their intermittent nature.
Nuclear fusion is the atomic process through which lighter atomic nuclei merge to form heavier ones. To initiate a fusion reaction, nuclei must be brought into extremely close proximity at minuscule distances, on the order of 10^{-15} meters. At this microscopic scale, the strong nuclear force overcomes electrostatic repulsion, enabling the fusion reaction to occur. Achieving such tiny inter-atomic distances necessitates providing the nuclei with very high kinetic energy, which in turn demands elevating the temperature substantially. Consequently, it's imperative to heat the light nuclei to exceedingly high temperatures. The energy needed to initiate fusion and the necessary temperature depend on the specific elements under consideration, particularly on its cross section σ. The latter quantifies the efficiency of the fusion reaction as function of the center-of-mass energy of the two reacting particles, measured in energy units. This concept is visually illustrated in Figure 1.1.

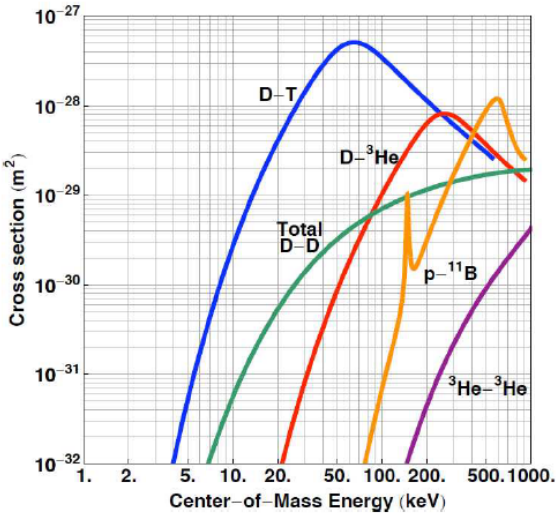

Figure 1.1: Cross section σ of the different reactions specified in equation 1.1. Notice that with "Total D-D" is indicated the sum of the cross section for both the D-D reactions. [1].

$$\begin{aligned}
\mathrm{D} + \mathrm{T} &\longrightarrow \mathrm{He}^3 + \mathrm{n} + 17.6\ \mathrm{MeV} \\
\mathrm{D} + \mathrm{D} &\longrightarrow \mathrm{T} + \mathrm{p} + 4.03\ \mathrm{MeV} \\
\mathrm{D} + \mathrm{D} &\longrightarrow \mathrm{He}^3 + \mathrm{n} + 3.27\ \mathrm{MeV} \\
\mathrm{D} + \mathrm{He}^3 &\longrightarrow \mathrm{He}^4 + \mathrm{p} + 18.3\ \mathrm{MeV} \\
\mathrm{He}^3 + \mathrm{He}^3 &\longrightarrow \mathrm{He}^4 + 2\mathrm{p} + 12.9\ \mathrm{MeV} \\
\mathrm{p} + \mathrm{B}^{11} &\longrightarrow 3\mathrm{He}^4 + 8.7\ \mathrm{MeV}
\end{aligned} \tag{1.1}$$

As can be notice, the most feasible reaction is the one between deuterium and tritium.
As previously mentioned, in order to make fusion reaction occur, it is necessary to raise the temperature of the deuterium and tritium mixture to a very high level, on the order of 100 million kelvin. At these temperatures, the gas mixture exists in a plasma state, where electrons are stripped from the nucleus due to intense thermal excitation. This creates an ionized gas, where nuclei and electrons are free to move. To ensure that the fusion reaction yields more energy than what is required to initiate it, it is necessary to respect the Lawson (or ignition) criterion, as expressed in the equation 1.2.

$$n \cdot \tau_E \cdot T \geq 3 \cdot 10^{21}\ \ \mathrm{KeV\,s/m^3} \tag{1.2}$$

where n is the density of the plasma density, T is its temperature and τ_E represent the energy confinement time.
Over the years, various methods for confining the plasma while simultaneously meeting the ignition criterion have been studied. The confinement methods primarily investigated are:

- **Inertial confinement**. A tiny sphere (approximately 2.5 mm in diameter) containing the mixture of deuterium and tritium is bombarded with a laser beams, compressing the mixture in a controlled implosion.

- **Magnetic confinement**. This is the most commonly used method and the one explored in this work. This type of confinement exploits the plasma's sensitivity to magnetic fields. In fact, the ions that make up the plasma are electrically charged and experience a Lorentz force when subjected to a magnetic field. Therefore, coils are used to generate high magnetic fields to confine the plasma.

Regarding the method of magnetic confinement, several types of reactors have been developed. The most widespread and utilized ones are the tokamaks and stellarators (Figure 1.2a and 1.2), devices with toroidal geometry. In these reactor types, to achieve a balance between the plasma's pressure forces and the magnetic forces, it is necessary to have a rotation of the magnetic toroidal field. The fundamental and structural difference between the two reactor types lies in the method used to generate this rotation of the toroidal magnetic field. In the case of tokamaks, a poloidal magnetic field is generated by a toroidal plasma current, while in the case of stellarators, the toroidal axis is physically rotated.

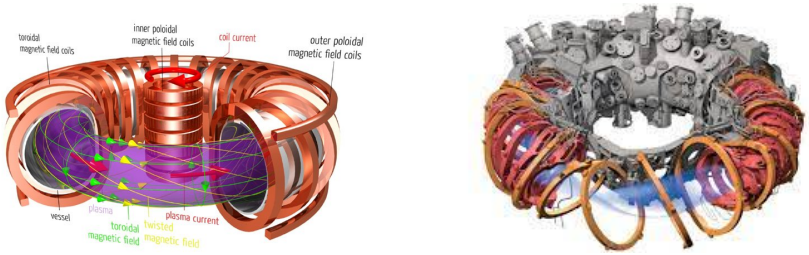

(a) **(b)**

Figure 1.2: Schematic representation of a tokamak (left)[2] and a stellarator (right)[3].

Due to the more complex toroidal geometry required to control the plasma, stellarators have so far been less successful than tokamaks.

1.2 The tokamak

The term "Tokamak" is an acronym derived from *TOroidal'naha KAmera s MAgnitnymi Katushkami*, which translates to "toroidal chamber with magnetic coils". This innovative device made its debut in Russia in the early 1950s and was officially introduced to the world during the International Conferences on the peaceful use of atomic energy held in Geneva. The tokamak consists of various distinct regions and apparatus, each of which can be further subdivided based on its specific function. An illustration of the ITER tokamak, the upcoming nuclear fusion reactor presently in the construction phase in Cadarache (France), is displayed in Figure 1.3. The diagram is followed by a comprehensive list and discussion of its diverse components is presented below.

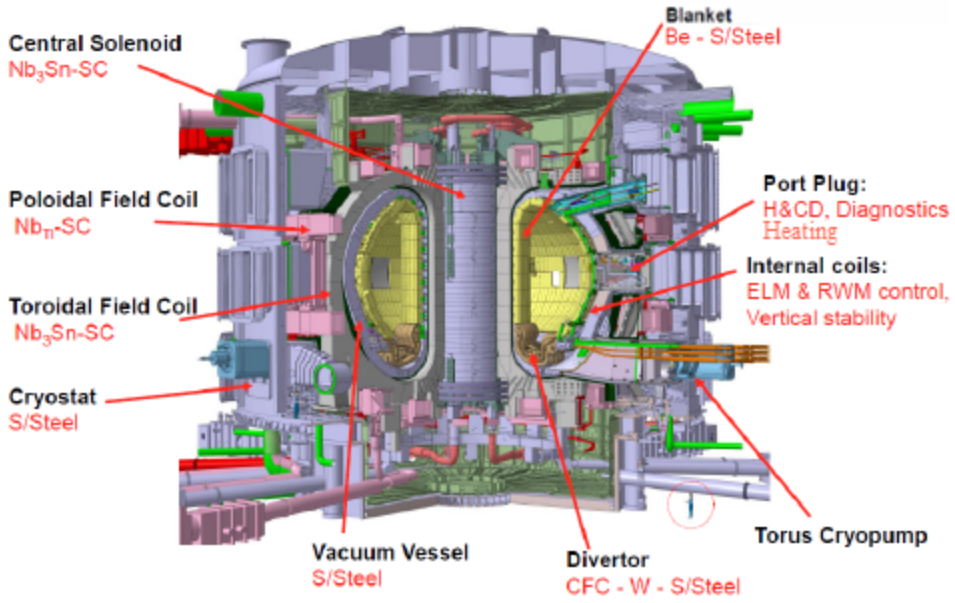

Figure 1.3: Schematic view of the ITER tokamak. [4].

- **Vacuum vessel** (VV). The vacuum vessel, constructed as a hermetically sealed, torus-shaped steel container, functions as the primary containment shield for the fusion reaction. Its dimensions directly impact the volume of the fusion plasma, consequently influencing the potential power output. To facilitate access for heating systems, diagnostics, and remote maintenance equipment, a specific set of ports are strategically distributed across the surface of the VV.

- **Magnets**. As mentioned, in a tokamak the magnets produce the magnetic field that confines the plasma and prevents it from contacting the walls. There are basically four type of magnets subsystems:
  - **Central Solenoid** (CS). It acts as a transformer, where a time-varying voltage is applied, creating a varying current in the plasma. In turn, the plasma generates a poloidal magnetic field according to Ampere's law. This field is responsible for maintaining plasma equilibrium and partially contributes to its heating.
  - **Poloidal Field Coil** (PC). Situated at various heights in the toroidal plane, are ring-shaped and primarily responsible for controlling the positioning and contouring of the plasma through the generation of a vertical component of the magnetic field.
  - **Toloidal Field Coil** (TC). The D-shaped magnets are positioned in the poloidal plane enclosing the plasma, producing the toroidal component of the magnetic field when electric current passes through them.
  - **Internal Coils**. They produce a field necessary to enhance the stability of the plasma and control it in case of disruptions, an abrupt loss of confinement.

- **Cryostat**. A massive stainless steel container that envelops the VV and the superconducting magnets. Within it, a high-vacuum environment is maintened by specific cryopumps, essential for plasma stability and for the functionality of the magnets. Additionally, it offers both radiation shielding and structural support for in-vessel components.

- **Heating system**. To initiate the fusion reaction within the VV, the injected gas must reach temperatures approaching 100 million Kelvin. While the ohmic heating from the plasma current is insufficient for this purpose, additional external heating methods are employed. These include neutral beam injection, where high-speed neutral hydrogen atoms transfer energy to the plasma as they decelerate, and high-frequency electromagnetic wave sources that induce oscillating currents in the plasma. The long-term objective is to achieve a self-sustaining burning plasma, therefore eliminating the dependence on external heating.

- **Divertor**. This represents a crucial element for exhausting the heat coming from the plasma. While neutrons are not affected by the magnetic field, charged particles remain confined within the plasma. The power deposited by these particles must be disposed of. Through the utilization of an extra toroidal coil, the charged particles are directed downwards to the lower section

of the VV, where they interact with the divertor walls. As a result, the divertor necessitates exceptional durability and efficient cooling measures.

- **Blanket**. A metal mantle that separates the plasma from the superconducting magnets. Indeed, the walls that directly interface with the plasma are referred to as the First Wall. Besides thermally isolating the plasma from the rest of the reactor, it serves the function of slowing down and shielding the neutrons resulting from the fusion process. Additionally, to generate electrical energy, it is necessary to extract thermal energy from the neutron slowing down, as they are the only particles capable of escaping the produced magnetic fields. This process would always be the responsibility of the blanket, given its shielding function. Finally, the last task assigned to this component would be tritium generation.

- **Diagnostics**. These instruments are essential for obtaining the measurements required to regulate plasma performance and to gain a deeper insight into plasma physics.

1.3 Spherical tokamak and ST40

A spherical tokamak (ST) is a variation of the tokamak fusion device characterized by an extremely low aspect ratio denoted as R/a, with R and a representing, respectivly,the major radius and the minor radius of the plasma. Typically, STs exhibit an aspect ratio that is below 1.8, as illustrated in Figure 1.4, which provides a visual contrast between the ST configuration and the conventional one. The concept of ST was originally developed at the UKAEA Culham, notably through the operation of the Small Tight Aspect Ratio Tokamak (START) experiment, which ran from 1991 to 1998.

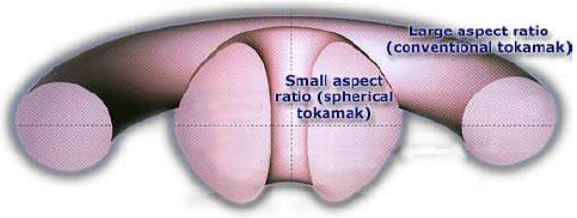

Figure 1.4: Comparison of the aspect ratios of a conventional tokamak and a spherical tokamak[5].

STs offer several advantages, which are:

- **Operation at high** β_t. A key indicator of a tokamak's performance is the parameter β, defined as the ratio of plasma pressure p to magnetic pressure. it can be experssed by:

$$\beta = \frac{p}{B^2/2\mu_0} \tag{1.3}$$

  where B is the magnetic field and μ is the magnetic permeability of the vacuum. In particular, β_t is obtained considering only the toroidal magnetic field, usually denoted with B_Φ. Physically, β_t

  represents the amount of plasma pressure that can be sustained by the magnetic field, so a higher value indicates higher fusion power. Therefore, β_t significantly influences the cost of electricity generated by fusion power, as the production of the toroidal magnetic field is a costly process. Therefore, a higher β_t value signifies a more efficient and economical tokamak design.

- **Enhanced stability**. STs devices exhibit naturally high elongation κ of the plasma. The latter quantifies how different is the shape of the plasma from a perfect circular one. The parameter κ is directly proportional to the safety factor q. This quantifies the extent of twisting in the field lines. It represents the average number of toroidal revolutions a field line needs to undergo to complete one poloidal revolution. A higher q indicates a smoother twist in the field line. Moreover, this enhances the MHD (magnetohydrodynamics) stability of the plasma.

- **Lower halo currents during disruptions**. Halo currents occur during plasma disruptions and channel large amounts of electrical current from the plasma to the vessel walls. The associated intense heat and particle fluxes can lead to erosion and damage of the materials comprising the vessel walls and other plasma-facing components. Recent evidence suggests that halo currents in STs might be comparatively smaller than those observed in conventional tokamaks. Furthermore, these currents appear to exhibit a more uniform distribution[6].

- **Potentially high bootstrap fraction**. The bootstrap current arises due to a plasma's pressure gradient, resulting in particle density fluctuations. These density gradients create an electric field, that guides the current. Remarkably, the bootstrap current's orientation yields a magnetic field that reinforces plasma confinementand enhance its stability. A greater proportion of bootstrap current reduces the necessity for costly non-inductive methods to drive current (such as neutral beam injection or radio frequency heating), thereby facilitating stable operational conditions and costs.

On the other hand, the STs present some disadvantages, in particular regarding the starp-up phase. This problems arise from the limited space dedicated to the

central solenoid. In this sense, research are focusing on non-inductive techniques, such as merging and compression[7] to start the plasma operation. Moreover, the engineering complexity involved in the construction and operation of ST can be significant. Achieving the necessary magnetic confinement and stability for sustained fusion reactions can require intricate design solutions, complex manufacturing processes, and advanced engineering techniques. This complexity can lead to increased construction costs and technical challenges.

There are more than twenty ST devices operating worldwide; stands out among these ST40, the privately funded, high-field spherical tokamak, owned and operated by Tokamak Energy Ltd. A schematic view of the tokamak is pictured in Figure 2.1, while the physical characteristics are listed in Table 1.1.

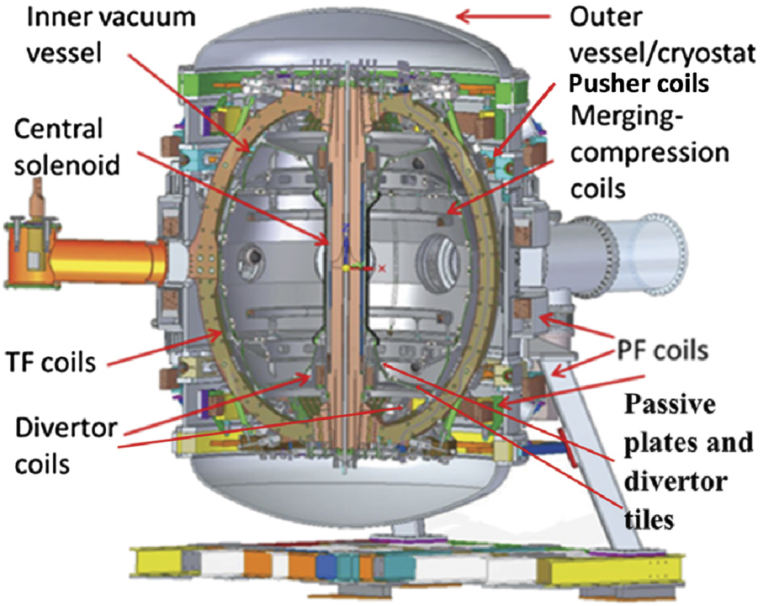

Figure 1.5: Cross-section view of ST40[8].

Minor radius	0.2 m
Major radius	$0.4 - 0.5$ m
Aspect ratio	$1.6 - 1.9$
Plasma current	$0.4 - 0.8$ MA
Toroidal magnetic field	$1.5 - 2.2$ T

Table 1.1: Main parameters of the ST40 tokamak [9].

The plasma is heated by two neutral beams injected tangentially in the same direction, delivering 0.9 MW at 55 MV and 0.7 MW at 24 MV when working with deuterium. For plasma start-up is used a merging compression technique, initiated by two high-voltage in-vessel poloidal field coils. This method enables direct access to high plasma currents without relying too much on the central solenoid. In fact, only a smaller central solenoid, providing approximately 200 mVs of inductive flux, is used to further boost the plasma current and maintain a flat-top current for up to 200 ms. For what regards the diagnostic system, ST40 is equipped with a complete set of magnetic field and flux sensors that allow the real-time control and post-pulse magnetic reconstruction. The electron density is measured using two sub-millimeters, both positioned at the midplane but one directed towards the radial direction and one in the tangential one. For the monitoring of impurities and Bremsstrahlung radiation, a full set of spectometers and line-filtered diodes is employed. Furthermore, three cameras look inside the plasma chamber: an infrared camera, a high-resolution fast visible and D-α camera; the latter is further treated in Section 2.1.

1.4 Purpose and structure of this thesis

The scope of this thesis, carried out in collaboration with Tokamak Energy Ltd, is to retrieve the neutral density distribution in the plasma chamber from the data extracted from the D-α camera. For this purpose, the CHERAB code was used[10]. An analitical neutral distribution was initially guessed, based on physical considerations as specified in [11] and further investigated in 2.2, which rely on numerous free parameters. These latter must be optimized to actually match the experimetal results. To find the best values, Bayesian optimization procedure was used.

In the next chapter, the physical and numerical background is explained, with particular focus on the Bayesian optimizator theory. Than, the results of the optimizator are presented for two different plasma shots.

Chapter 2

Theorethical background

2.1 The D-α camera

According to the Bohr atomic model, the energy of an electron in an atom orbit assumes discrete values, called energy levels. As an electron transitions from a higher energy level to a lower one, it emits a photon with energy equivalent to the difference in energy between the two levels. Therefore, the photon emitted must assume discrete values of energy, which fixed the frequency (or the wavelength) of the light emitted. The sum of all the possible transition for an electron in a atom is called spectrum. The term $D-\alpha$ emission refers to a specific spectral line in the deuterium atom's emission spectrum. In particular, this spectral line results from the transition of an electron from the third energy level ($n = 3$) to the second one ($n = 2$). The energy of the emitted photon is 1.9 eV, which corresponds to a wavelength of 656.28 nm, thus can be observed as red light.

It is important to clarify that this emission pertains only neutral deuterium atoms. In a tokamak, due to the high temperature, plasma is created where electrons and nuclei are separated. Nevertheless, also neutral atoms are present due to plasma neutralization at the wall[12]. When an ions strike to the wall, it tends to stick to it long enough to recombine with an electron that is present on the surface. Consequently, the resulting neutral atom are weakly bounded to the surface and is emitted back in the plasma chamber. This process takes also the name of *plasma recycling*.

The neutrals emitted from the wall are in the ground state, that is the lowest energy state that its electrons can occupy. Neutrals can be excited mainly due to elastic collision with the plasma particles (ions and electrons) and with other neutrals. Another source of neutrals is the plasma recombination: ions recombine

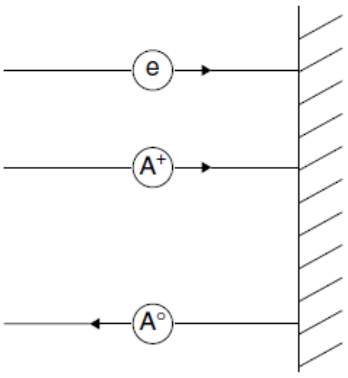

Figure 2.1: Schematic visualization of the plasma recycling process at the wall of a tokamak.[12].

with an electron close to them:

$$D^+ + e^- \rightarrow D \tag{2.1}$$

The D-α camera is a device able to capture the photons emitted from the electron transition from $n = 3$ to $n = 2$. In this thesis, two images coming from two different plasma shots are analysed. In Figure 2.2 it is shown the the D-α camera view for shot 9229 at 65 ms, while in Figure 2.3 the results from the shot 10041 at time 17 ms.

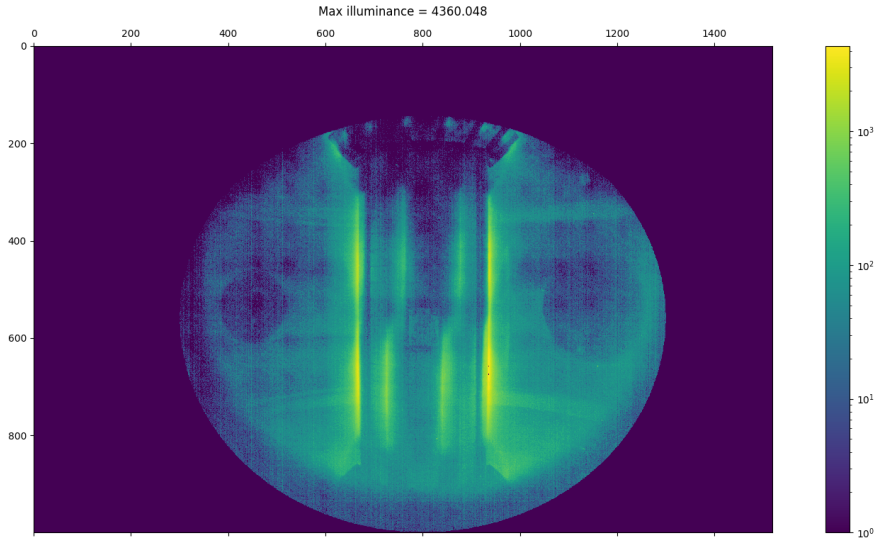

Figure 2.2: D-α camera view for shot 9229 at 65 ms.

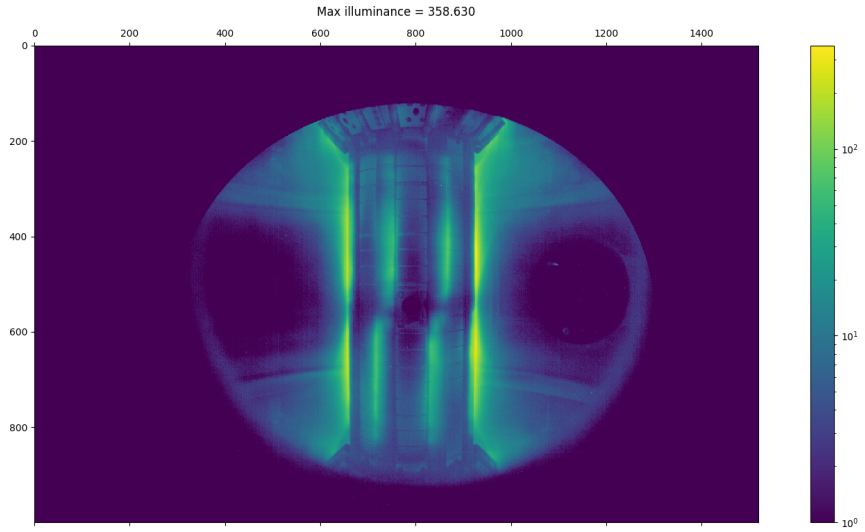

Figure 2.3: D-α camera view for shot 10041 at 17 ms.

Both plasma shots, produced in the same experimental campaign, reveal similar features:

- **Limited scenario**. The plasma is limited to the center column and the emission is concentrated in the proximity of the 8 discrete limiters.
- **Up-down asymmetry**. The emission is concentrated in the lower part of the limiter. This is due to the asymmetry in the magnetic coil setup. This is really a key aspect if we want a perfect match with the simulation results.
- **Divertor emission**. The emission not only comes from the limiters, but also from the passive plates positioned at the top and at the bottom of the central column.

2.2 Numerical modelling

2.2.1 The CHERAB code

CHERAB[10] is the Python library used for forward modelling diagnostics based on spectroscopic plasma emission. It is constructed over the Raysect library[13], a ray-tracing engine for geometrical optics applications. A ray tracer is an algorithm designed to simulate the propagation of light, treating it as a bundle of rays moving through a scene. The scene is made by 3D-modelled solid objects and media which can both absorbe, diffuse, reflect or refract the light. In this

work, the objects are limited to perfectly absorbing surfaces or isotropic radiation sources. Moreover, the assumption of optimical thin medium is made for the plasma[14]. The rays travel in straight lines until they encounter objects in the scene. When interacting with materials, a contribution on emission is either added or subtracted from the rays depending on the properties of the materials. The process of ray tracing can be bidirectional, running in both forward and reverse directions. In forward ray tracing, light is traced from sources through material interactions to the observing surface, while reverse ray tracing works in the opposite direction. The latter is generally less computationally expensive and it is the one that Raysect normally use. Therefore, given an observing surface, the origins of the rays straight lines are uniformly distributed all over it. Instead, the directions are sampled through various methods; the most used ones are cosine-like distribution across a hemisphere and uniform distribution within a cone. Than the algoritm tests each ray for intersection with the object in the scene. Finally, relying on a Monte-Carlo integration the samples are integrated in space all over the rays to give the final output, which depends by the source specified (see Subsection 2.2.2).

The architecture of the CHERAB code is presented in Figure 2.4. As can be seen, CHERAB utilizes a Raysect engine as its foundation, which defines core ray-tracing functionalities and mesh handling. In the Core API Module are specified all core functionality such as: how plasmas are defined, properties computed from them, types of atomic data for spectroscopic calculations and the range of plasma emissions that can be computed. Finally, in the user packages layer are present libraries organized as scripts for particular study.

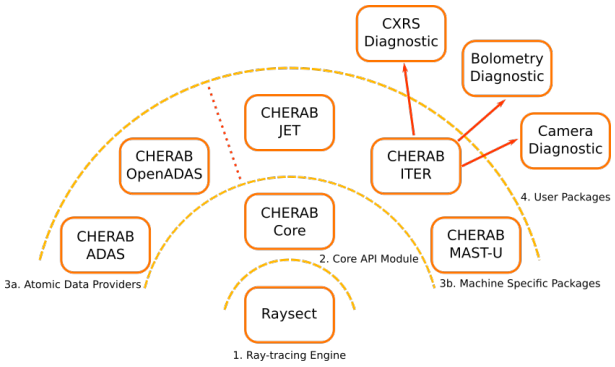

Figure 2.4: Onion shells CHERAB structure.

2.2.2 Simulation setup

In this section is presented the simulation setup used for the reproduction of the D-α camera. The framework is basically identical to the one presented in [11], of which this work represents an extension. However, it is crucial to investigate deeply the configuration in order to understand the role of the optimization procedure. First of all, it is necessary to have a D-α radiation emission source. To construct it, *analitical* model of plasma profiles of density and temperature, together with neutral density is used as input to compute the fractional abundance of deuterium with the electron in the third energy level using the Amjuel database[15]. For the plasma, the assumption of identical ions and electron temperature $T_e = T_i = T$ and density $n_e = n_i = n$ is made. All the profiles are built using the normalised poloidal flux coordinate ψ_N, calculated as :

$$\psi_N = \frac{\psi - \psi_0}{\psi_{sep} - \psi_0} \tag{2.2}$$

where ψ is the magnetic flux in the given location, ψ_0 and ψ_{sep} are ,respectivily, the magnetic flux at the magnetic axis and at the LCMS. The magnetic equilibrium is reconstructed using EFIT[16]. A Gaussian shape centred on the magnetic axis ($\psi_N = 0$) is assumed for both temperature T_e and density n_e core plasma profiles.

$$n_e^{core} = n_e^{\psi_N=0} \cdot \exp(-\psi_N^2/2\sigma_n^2) \qquad 0 \geq \psi_N \leq 1 \tag{2.3}$$

$$T_e^{core} = T_e^{\psi_N=0} \cdot \exp(-\psi_N^2/2\sigma_T^2) \qquad 0 \geq \psi_N \leq 1 \tag{2.4}$$

For the shot 9229, the density $n_e^{\psi_N=0}$ and temperature $T_e^{\psi_N=0}$ at the magnetic axis are fixed from the experimental data. Instead, for the shot 10041 these data where not available. The σ parameters in the Gaussian expressions are calculated as:

$$\sigma_n = \left[2\ln(n_e^{\psi_N=0}/n_e^{\psi_N=1})\right]^{-1/2} \qquad \psi_N > 1 \tag{2.5}$$

$$\sigma_T = \left[2\ln(T_e^{\psi_N=0}/T_e^{\psi_N=1})\right]^{-1/2} \qquad \psi_N > 1 \tag{2.6}$$

The value of plasma density $n_e^{\psi_N=1}$ and temperature $T_e^{\psi_N=1}$ at the LCMS are fixed to reasonable values obtained from [12]. For the edge plasma, exponential decay in the radial direction is assumed for both the profiles. Moreover, the plasma is assumed to be isothermal in the poloidal direction, while the density follow the 2-point model[12]. The function $F(\theta)$ is used to make the density doubles when moving from the outer mid-plane to the wall.

$$n_e^{edge}(\psi_N, \theta) = \max\left[n_e^{\psi_N=\infty}; n_e^{\psi_N=1} \cdot \exp(-(\psi_N - 1)/\lambda_n^{\psi_N}) \cdot F(\theta)\right] \tag{2.7}$$

$$T_e^{edge}(\psi_N) = \max\left[T_e^{\psi_N=\infty}; T_e^{\psi_N=1} \cdot \exp(-(\psi_N - 1)/\lambda_T^{\psi_N})\right] \tag{2.8}$$

For the parameters $\lambda_n^{\psi_N}$ and $\lambda_T^{\psi_N}$ are assumed values in order to reproduce the estimation present in [12]. Instead, the value of $n_e^{\psi_N=\infty}$ and $T_e^{\psi_N=\infty}$ are fixed respectivily to 10^{-14} m^{-3} and 0.1 eV. One and two dimensional plots of the resulting plasma density and temperature are presented in the following figures.

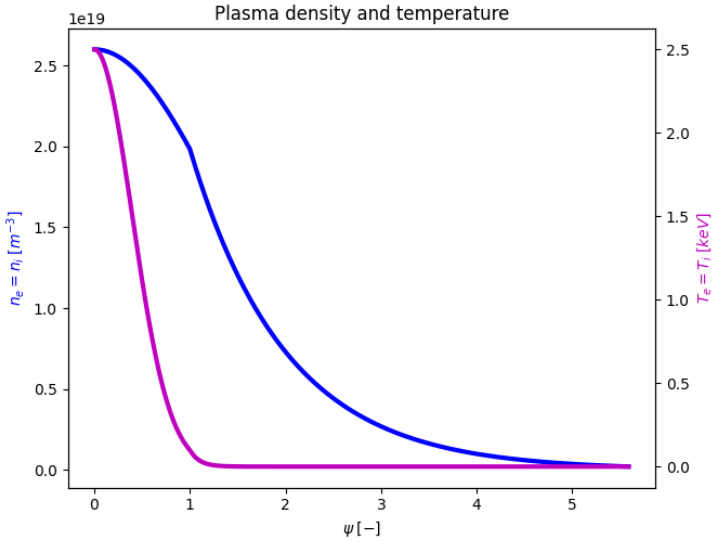

Figure 2.5: One dimensional profiles of the plasma density (blue) and temperature (purple).

For what regards the neutral density, no distinction has been made between molecules and atoms. The profile is given by the superposition of two distinct contribution:

- A background (BG) profile which monotonically increase with the magnetic flux coordinate, described by the equation:

$$n_g^{BG}(\psi_N) = n_g^{\psi_N=0} + (n_g^{\psi_N\to\infty} - n_g^{\psi_N=0}) \cdot [1 + \exp(-(\psi_N - 1)/\mu_g)]^{-1} \quad (2.9)$$

  where the parameter μ_g quantify the sharpeness of the transition between the edge and the core. A one dimensional profile is showed in Figure 2.8.

- To simulate the limiter recycling process, two Gaussian are added to the background density. The latters are positioned at the strike points (R_s and Z_s are the radial and axial position) , retrieved in a qualitative way. Each of these is described by the equation:

$$n_g^R(\psi_N) = n_{g,0}^R \cdot \exp(-(R - R_s)^2/2\sigma_{g,R}) \cdot \exp(-(Z - Z_s)^2/2\sigma_{g,Z}) \quad (2.10)$$

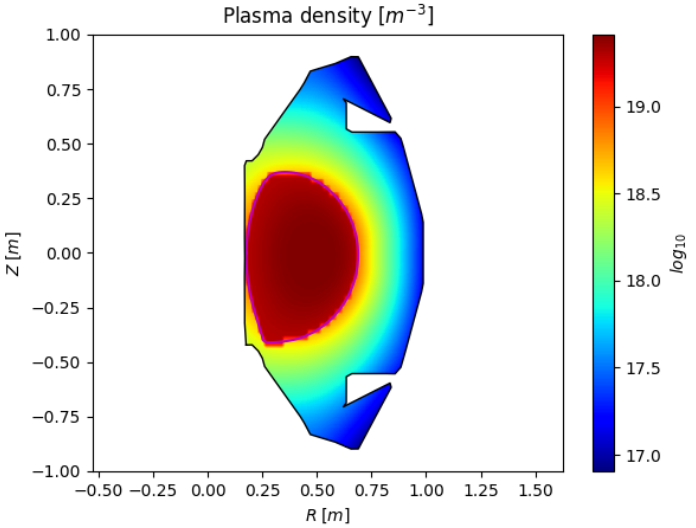

Figure 2.6: Two dimentional distribution of the plasma density in logaritmic scale.

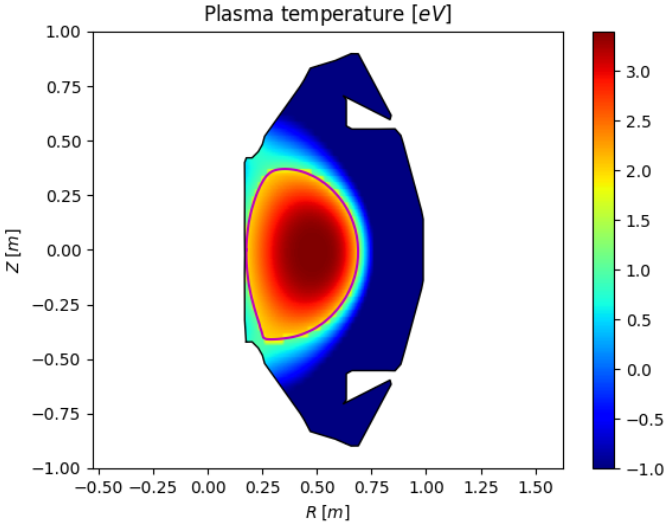

Figure 2.7: Two dimentional distribution of the plasma temperature.

The parameters $\sigma_{g,R}$ and $\sigma_{g,Z}$ are chosen according to the ionization mean free path, that is larger in the axial direction respect to the radial one.

The resulting neutral density is illustrated in Figure 2.9.

Moreover, to allow a complete comparison with the experimental data, a neutral

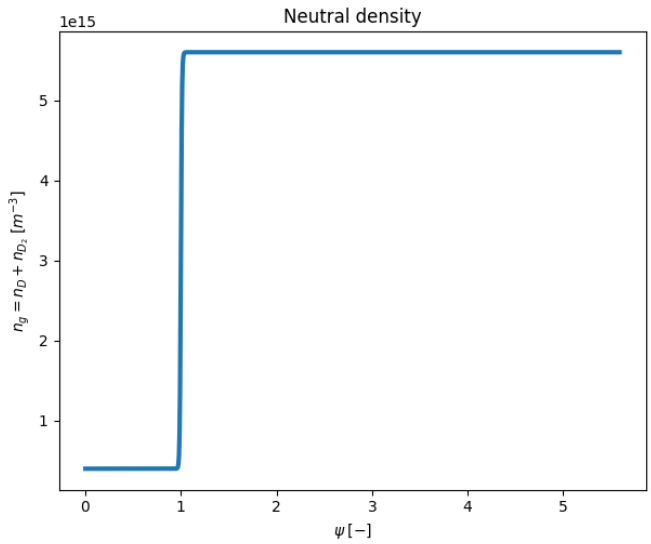

Figure 2.8: One dimensional reproduction of the background neutral density.

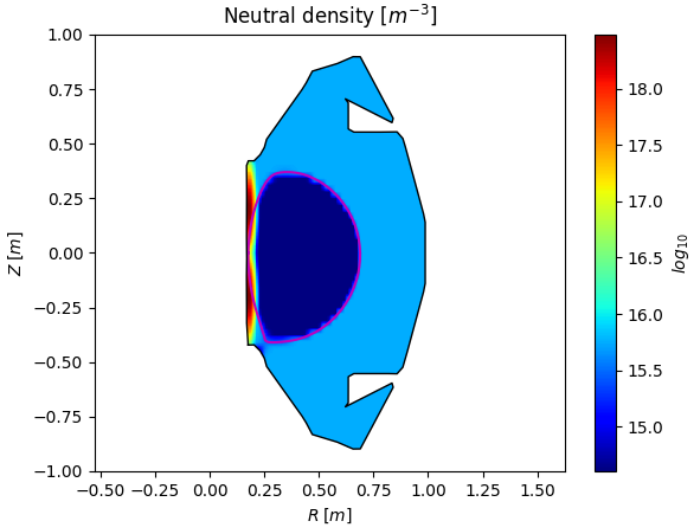

Figure 2.9: Two dimensional distribution of the deuterium neutrals in logaritmic scale.

density source in added in the same fashion of the limiter one in the proximity of the upper and bottom passive plates. As can be noticed, all the proposed analitical models have user-define free parameters that must be choosen in order to represent

correctly the experimental data, with remaining consistent with the physics. For example, the plasma temperature at the separatrix $T_e^{\psi_N=1}$ has been choosen equal to 100 eV in [11] but it is arbitrary. A value of 150 eV or 50 eV is still physically acceptable. Therefore, the discriminant within the possible value must be the correct reproduction of the experimental data. This because the actual objective of this analysis is to infer neutral parameters. In this sense, Bayesian optimization can be a suitable tool for identify the best values and, consequently, obtaining the best inference.

Once the neutral density, plasma density and temperature has been computed it is possible to use the Amjuel database to obtain the fractional abundance of deuterium with the electron in energy level $n = 3$, showed in Figure 2.10. Finally, simply using the transition probability for $n = 3 \rightarrow n = 2$, given by [17], it is possible to obtain the two dimensional D-α source, expressed in [ph $\mathrm{m}^{-3}\mathrm{s}^{-1}$] and illustated in Figure 2.11. The latter is then transformed in a three dimensional radiation source using the piece-wise emission distribution presented in [11]. Furthermore, an additional feature has been implement to better reproduce the experimental data. In fact, the emission in the regions next to the limiters is not exactly null, but decrease rapidly when moving away from them. To take into account this aspect, a radiation source is added in the non-limiter width, proportionally to the ionization mean free path of the neutrals calculated using Amjuel.

Finally, the source is sampled in CHERAB providing a result in [ph $\mathrm{m}^{-2}\mathrm{s}^{-1}\mathrm{sr}^{-2}$]. To allow the comparison with the experimental data, the output is firstly converted in [Wm^{-2}] and than in illuminance using the conversion formula specified in [18].

2.2.3 Complete list of the parameters

A complete list of the free parameters present in analitical models is presented. For each of them, is presented its physical meaning and the corrisponding reasonable boundaries. These are than use as bound of the search space in the Bayesian optimization.

- $n_g^{\psi_N=0}$. Neutral density in the core. Bounds $[10^{13}, 10^{15}]$ m^{-3}
- $n_g^{\psi_N\rightarrow\infty}$. Neutral density in the edge. Bounds $[10^{14}, 10^{16}]$ m^{-3}
- μ_g. Sharpness of the background neutral density. Bounds $[10^{-4}, 10^{-2}]$
- $\sigma_{g,R}$. Variance of the limiter Guassian in the radial direction. Bounds $[10^{-5}, 10^{-3}]$
- $\sigma_{g,Z}$. Variance of the limiter Guassian in the axial direction. Bounds $[10^{-3}, 10^{-1}]$

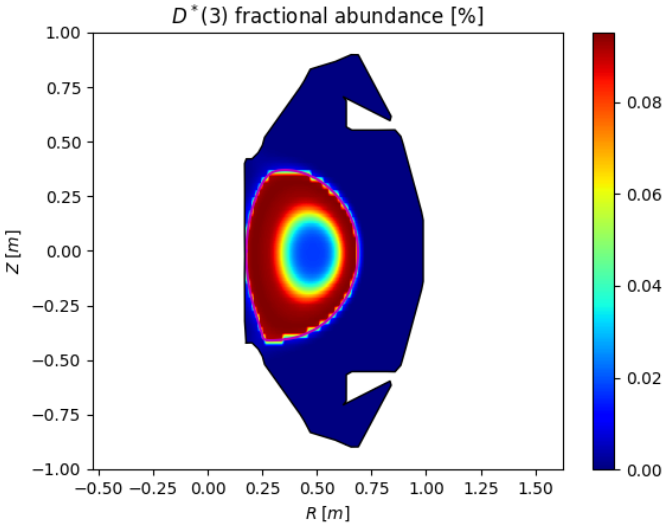

Figure 2.10: Fractional aboundance of deuterium with electron in $n = 3$.

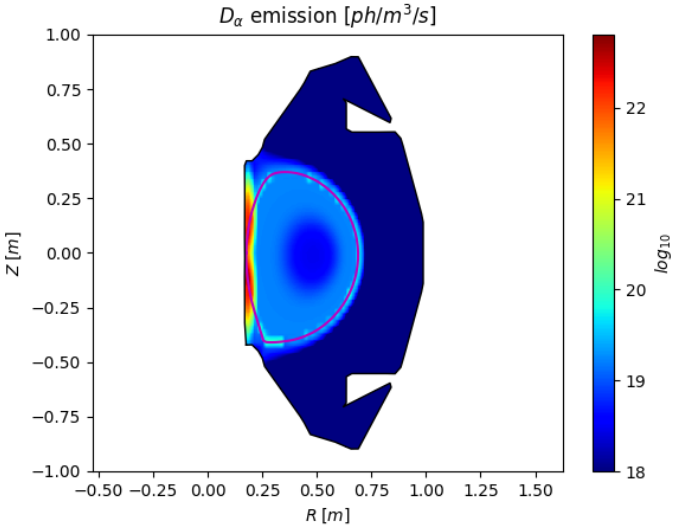

Figure 2.11: Two dimensional D-α emission source in logaritmic scale.

- $n_{g,0}^{R,upper}$. Peak value of the upper limiter Guassian. Bounds $[10^{17}, 10^{19}]$ m^{-3}
- $n_{g,0}^{R,lower}$. Peak value of the lower limiter Guassian. Bounds $[10^{13}, 10^{15}]$ m^{-3}
- R_s. Radial position of the strike point at the limiter. Bounds $0.15, 0.25]$ m

- Z_s^{upper}. Axial position of the upper limiter Gaussian. Bounds $[0.1, 0.3]$ m
- Z_s^{lower}. Axial position of the lower limiter Gaussian. Bounds $[-0.3, -0.1]$ m
- $n_{g,0}^{div,upper}$. Peak value of the upper divertor Guassian. Bounds $[10^{17}, 10^{19}]$ m^{-3}
- $n_{g,0}^{div,lower}$. Peak value of the lower divertor Guassian. Bounds $[10^{17}, 10^{19}]$ m^{-3}
- R_{div}. Radial position of the strike point at the divertor. Bounds $[0.2, 0.3]$ m
- Z_{div}^{upper}. Axial position of the upper divertor Gaussian. Bounds $[0.4, 0.5]$ m
- Z_{div}^{lower}. Axial position of the lower divertor Gaussian. Bounds $[-0.5, -0.4]$ m
- $\sigma_{g,R}^{div}$. Variance of the divertor Guassian in the radial direction. Bounds $[10^{-5}, 10^{-3}]$
- $\sigma_{g,Z}^{div}$. Variance of the divertor Guassian in the axial direction. Bounds $[10^{-3}, 10^{-1}]$
- $n_e^{\psi_N=1}$. Plasma density at the separatrix. Bounds $[10^{18}, 2 \cdot 10^{19}]$ m^{-3}
- $\lambda_n^{\psi_N}$. Plasma density decay length. Bounds $[10^{-1}, 5]$
- $T_e^{\psi_N=1}$. Plasma temperature at the separatrix. Bounds $[50, 150]$ eV
- $\lambda_T^{\psi_N}$. Plasma temperature decay length. Bounds $[10^{-2}, 1]$
- c_{upper}. Geometrical correction factor for the upper limiter Gaussian to take into account the asymmetry in the magnetic coil setup. Bounds $[0, 0.122]$
- c_{lower}. Geometrical correction factor for the lower limiter Gaussian to take into account the asymmetry in the magnetic coil setup. Bounds $[0, 0.122]$
- $c_{smoothing}$. Numerical factor to smooth the emission in accordance with the mean free path. Bounds $[10^{-3}, 10^{-1}]$

Moreover, for the simulation of the shot 10041 two additional parameters are inserted in the model:

- $n_e^{\psi_N=0}$. Plasma density at the center of the core. Bounds $[10^{18}, 4 \cdot 10^{19}]$ m^{-3}
- $T_e^{\psi_N=0}$. Plasma temperature at the center of the core. Bounds $[2500, 1000]$ eV

2.3 Bayesian optimization

As mentioned previously, employing analytical models to characterize neutral and plasma distribution represent a problem due to numerous free parameters that require precise selection. To address this issue, Bayesian optimization (BO) emerges as a possible solution[19]. It is a global optimization algorithm designed for optimizing functions that are expensive to evaluate and must be treated as black boxes. The simulation is expensive since require several minutes to execute, bearing in mind that the exact duration depends by the desired statistical precision.

For the optimization, the outputs from the simulations are summarized and combined with the experimental ones to form a target function $f(x)$ that expresses the difference between the numerical and the true data. $f(x)$ is treated like a black box since we don't know a priori its functional properties, like concavity or linearity that would make it easy to optimize using techniques that use this informations to improve efficency. The input variables x are points in the n-dimensional input parameter space listed in Table 104.

The BO algorithm is divided into two phases. Initially, the target function is modeled as a probability distribution of potential target functions, constained on the available data points. Subsequently, the second phase of BO involves the formulation of an acquisition function. This function is designed to guide the sampling process more efficiently than a random approach, guiding the optimization process strategically. For what regards the first part of BO algorithm, the target function is modelled Gaussian process (GP) regression; the approach is outlined in Subsection 2.16. Subsequently, the scope of the acquisition function is described in Subsection 2.3.2, with specific focus on improvement-based acquistion function. A comprehensive listing of all variables utilized throughout the remainder of the thesis is provided in Table 2.1.

x	Input data point
x_p	Input data prediction
y	Output data point
ϵ	Noise of the output data point
$f(x)$	Model function value at the input data point
$f(x_p)$	Model function value at predictive point
$\mu_0(x)$	Mean function of the GP
$\Sigma_0(x, x')$	Covariance function (or kernel) of the GP

Table 2.1: Variables used for explanation of the BO theory.

2.3.1 Gaussian process regression

In general, a model M can be defined as a process that produces observations based on an initial input dataset x. The resulting output, y, may be affected by the influence of noise. To address this variability, we decompose the output into a deterministic target function, $f(x)$, and the noise component ϵ.

$$M : y(x) = f(x) + \epsilon \tag{2.11}$$

The aim is to make correct inference about $f(x)$ and ϵ. In the framework of Bayesian inference, the prior knowledge of this quantities in incorpored in the model trought prior probability distribution. According to the Bayes theorem, we can evaluate the posterior probability distribution of the unknowns quantities given the observations and the model as:

$$P(f, \epsilon|y, M) = \frac{P(y|f, \epsilon, M)\ P(f, \epsilon|M)}{P(y)} \tag{2.12}$$

where $P(f, \epsilon|y, M)$ is the posterior probability, $P(y|f, \epsilon, M)$ is the likehood probability, $P(f, \epsilon|M)$ is the prior probability while $P(y)$ is a normalization coefficent called marginal likehood. In GP regression, the prior probability distribution of functions $f(x)$ is described by a Gaussian process, defined as[20]:

Definition 1 *A Gaussian process is a collection of random variables, any finite number of which have a joint Gaussian distribution.*

A GP can be seen as an infinite multivariate normal distribution, described by a mean vector $\mu_0(x)$ and a covariance function $\Sigma_0(x, x')$. Consequently, the prior

probability distribution of $f(x)$ can be written as:

$$f(x) \sim GP(\mu_0(x), \Sigma_0(x, x')) \tag{2.13}$$

In our case, the random variable is represented by the value of $f(x)$ given input point x. Therefore, we have something that is finite that must linked to something that is continuos, the function $f(x)$. This is possible thanks to the *consistency condition*, which imply that the joint distribution of a finite collection of random variables doesn't change if infinite variables are included in the distribution.

A GP is completely described by its mean and covariance function, defined as:

$$\mu_0(x) = \mathrm{E}[f(x)] \tag{2.14}$$
$$\Sigma_0(x, x') = \mathrm{E}[(f(x) - \mu_0(x))(f(x) - \mu_0(x)] \tag{2.15}$$

The kernel is selected in order to have a positive correlation between points that are close in the input space. This implies a belief that their function values should be more similar compared to points that are distant from each other. In this sense, the covariance function express how the input data are correlated. Moreover, it is possible to use periodic covariance function to incorporate periodic behavior of the target function $f(x)$. Therefore, the choice of this function is really important. Two of the most used covariance functions are the squared exponential (SE) and the Matérn. The SE has the form:

$$\Sigma_{SE}(x - x') = \exp(-\frac{-(x - x')^2}{2l^2}) \tag{2.16}$$

The parameter l is called lengthscale. As can be notice, as the distance between inputs increases relative to the lengthscale, the covariance approachs zero. Thus, the lengthscale express how sharp are the variations of the function compared to the one in the input variables. In Figures 2.12 and 2.13 are shown five functions sampled from a GP with mean equal to 0 and SE kernel (left) and the corresponding visualization of the covariance matrix (right) . From these, we can appreciate as how the functions show rapid variation to small difference in the input variance when the lengthscale is small. On the other hand, for bigger lengthscale the functions exhibit smoother behaviour.

Another really used covariance function is the Matérn. It is represented by:

$$\Sigma_M(r) = \frac{2^{1-\nu}}{\Gamma(\nu)}\Big(\frac{\sqrt{2\nu r}}{l}\Big)^{\nu} K_\nu\Big(\frac{\sqrt{2\nu r}}{l}\Big) \tag{2.17}$$

where $r = |x - x'|$ is the absolute distance between two input points, ν is called smoothness parameter, l is the lengthscale and K_ν is a modified Bessel function.

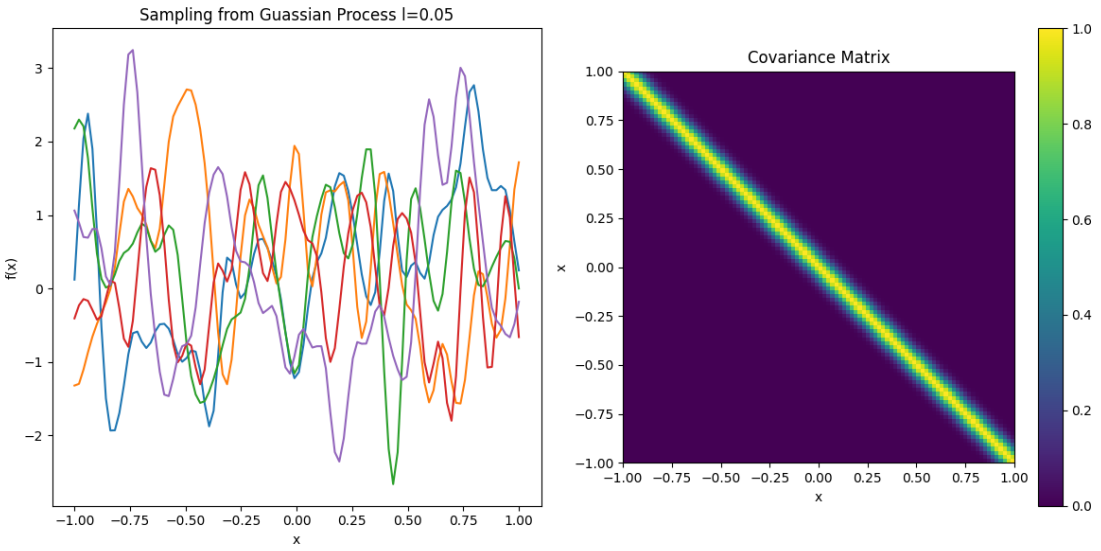

Figure 2.12: Five random samples from a Gaussian process characterized by SE kernels, with mean 0 and lengthscale 0.05.

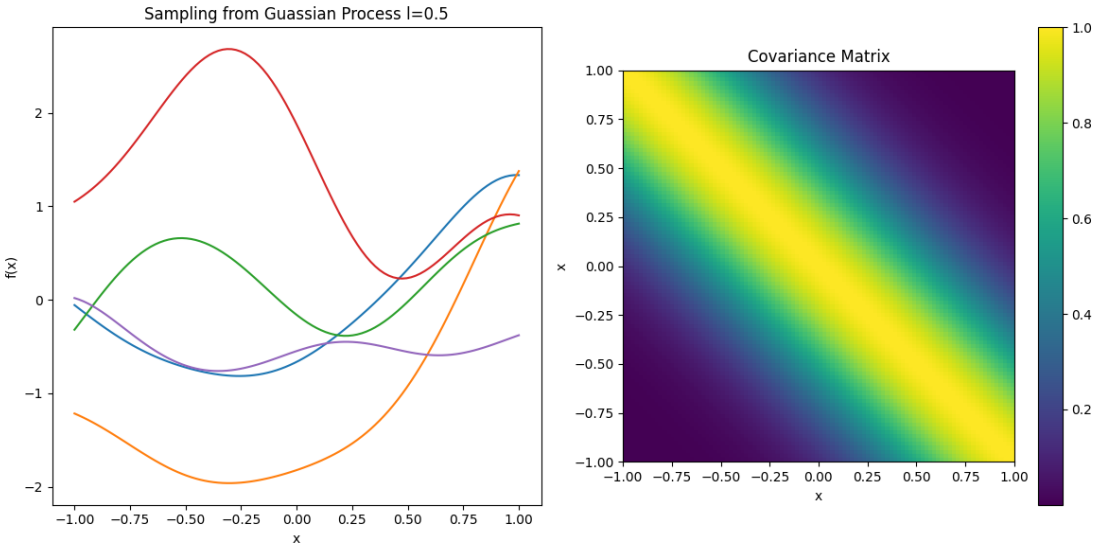

Figure 2.13: Five random samples from a Gaussian process characterized by SE kernels, with mean 0 and lengthscale 0.5.

The meaning of the lengthscale is the same of the SE kernel. On the other hand, the smoothness parameter,as the name suggest, express the regularity of the functions. Higher value of ν correspond to smoother curves, as can be seen from the comparison

between Figure 2.14 and 2.15.

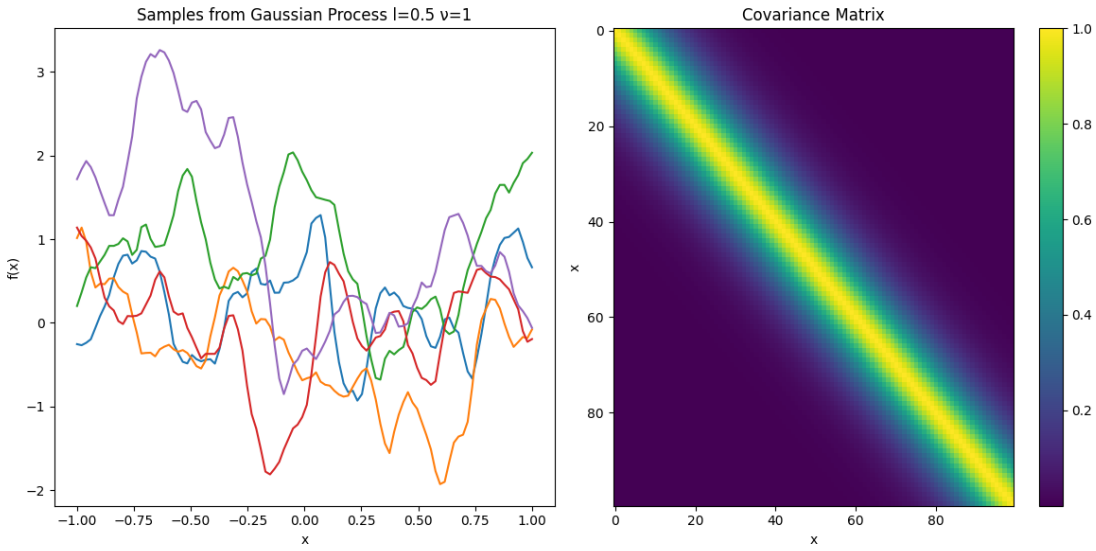

Figure 2.14: Five random samples from a Gaussian process characterized by Matérn kernels, with mean 0, $l = 0.5$ and $\nu = 1$

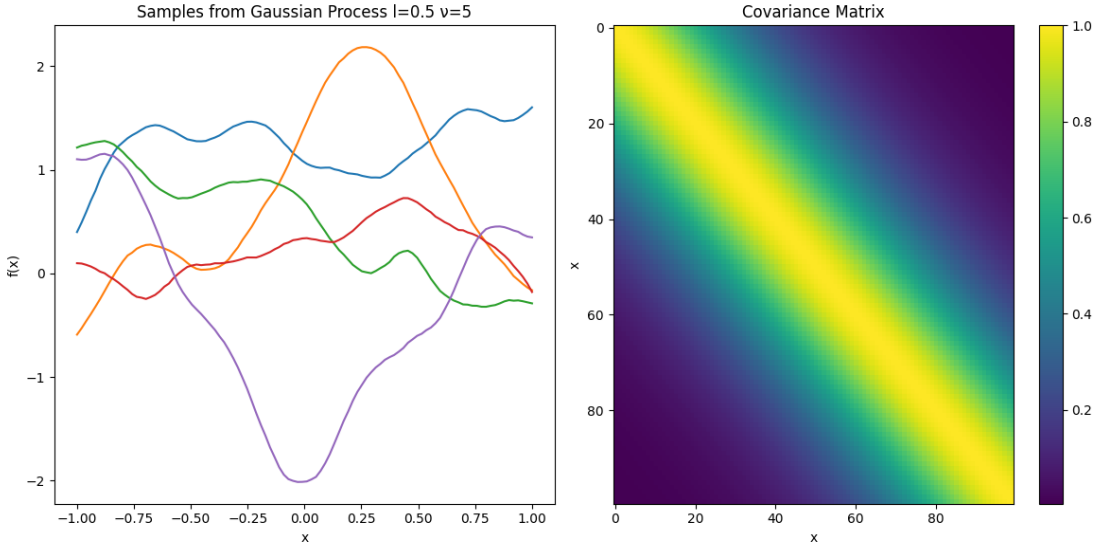

Figure 2.15: Five random samples from a Gaussian process characterized by Matérn kernels, with mean 0, $l = 0.5$ and $\nu = 5$

In literature, the lengthscale and the smoothness parameters are called hyper-parameters since they have influence on the prior distribution rather than on the

model itself. Nevertheless, they must be tuned by the GP in order to improve the knowledge about $f(x)$.

Until now, we focused on the modelling of the prior distribution of $f(x)$. In order to be able to calculate the posterior distribution, which is the one used to make predictions, we have calculate also the likehood and the marginal likehood distribution, as expressed in equation 2.12. The likelihood is the probability of measuring the observations y, given the model M, the target function $f(x)$ and the noise ϵ. Recalling equation 2.11, we have that the observation depends only the function and the noise. As discussed before, $f(x)$ is modelled as a multivariate normal with the GP. In the same vay, the noise ϵ can be described as multivariate normal distribution. Consequently, the observation y is represented as a multivariate normal, with mean function and covariance function equal to the sum of the ones for $f(x)$ and ϵ. Typically, the noise is assumed to have zero mean and the covariance function is built to have all the observation point uncorellated.

The marginal likelihood, also known as the evidence, is obtained by integrating (or marginalizing) the product of the prior and likelihood distributions over all possible function values.

$$P(y) = \int P(y|f,\epsilon)P(f,\epsilon)df d\epsilon \tag{2.18}$$

This integral is often impossible to treat, but in the context of GP, the algebraic properties of multivariate normal distributions allow for a closed-form expression, resulting in a computationally efficient formula. The marginal likelihood is often used for hyperparameter optimization. By maximizing the marginal likelihood with respect to the hyperparameters, one can find the set of hyperparameters that best explains the observed data.

Finally, the posterior distribution in equation 2.12 can be calculated. The latter represent our current knowledge about the target function and the noise and can be used to predict new data point y_{new}. The probability of y_{new} given the current observation y can be expressed as:

$$P(y_{new}|y) = \int P(y_{new}, f, \epsilon|y)df d\epsilon = \int P(y_{new}|f,\epsilon)P(f,\epsilon|y)df d\epsilon \tag{2.19}$$

In the same way , we can infer new function values f_{new} from the posterior predictive distribution, calculated as:

$$P(f_{new}|y) = \int P(f_{new}, f, |y)df = \int P(f_{new}|f)P(f|y)df \tag{2.20}$$

where $P(f|y)$ is the posterior marginalized over the noise. Since all the input distributions are multivariate normal, also the posterior predictive distribution will

be of the same kind. In Figure 2.16 is shown the final results of a GP regression for an initial samples of three points.

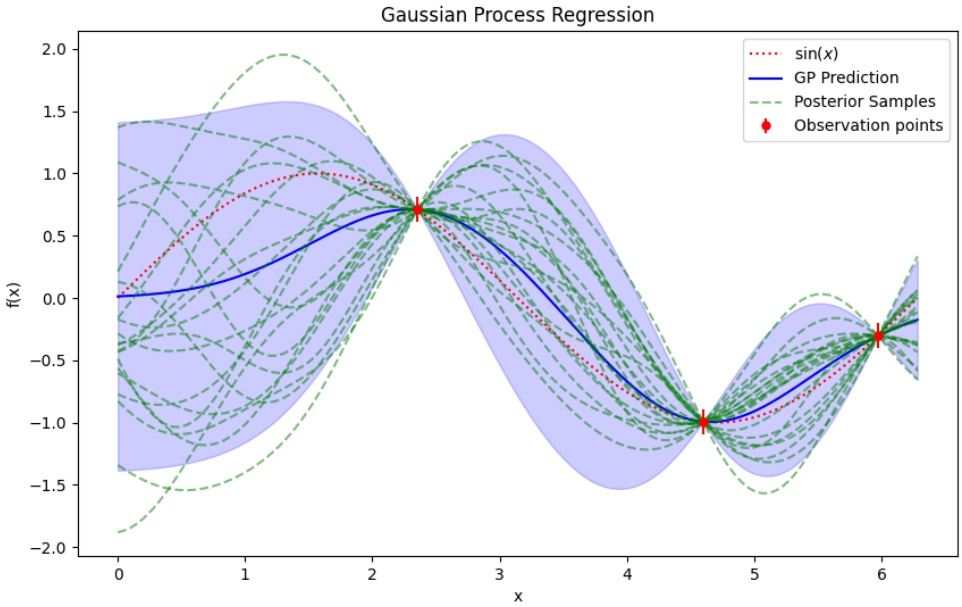

Figure 2.16: The posterior predictive distribution, conditioned on three data points sampled from the function $\sin(x)$ (red dots), is illustrated in the graph. The 20 drawn samples from the distribution are represented by green dashed lines, with the shaded region indicating two standard deviations and the blue line indicating the distribution's mean.

2.3.2 Acquistion function

Once we have modelled the target function using GP regression, the next step is to find the maximum. To do that an acquisition function is computed from the posterior predictive distribution. Afterwards, the maximum of the acquisition function is evaluated with standard optimization procedure, which will give the next input point to evaluate. Numerous strategies exist for definition of an acquisition function. In any case, it should be formulated in orfer to balance two important features:

- **Explotation**. Exploration involves searching for new regions of the parameter space, where the uncertainty of the model is important.

- **Exploration**. Exploitation is the process of focusing on the known regions of the parameter space. An acquistion function that prioritize explotation select point close to the actual maximum value.

The acquisiton function used in this work is the Expected Improvement (EI), which is also one of the most employed [19]. It quantifies the potential improvement of the objective function over the current best-known value at a particular point in the parameter space. In mathematical terms, the Expected Improvement at a point x is defined as:

$$EI(x) = \mathrm{E}[max(f(x_{best}) - f(x),0] \tag{2.21}$$

where $f(x_{best})$ is the best value found, $f(x)$ is GP regression model prediction at input value x. At the end, the point with the highest expected improvement is chosen as the next evaluation point.

2.3.3 TuRBO algoritm

BO performs well in on low dimensional problems (below than 20 input variables) and small sample budgets. However, this is not the case of the current work, since the dimensionality of the problem is higher (at least 23 parameters must be optimized). For this reason, has been used the Scalable Global Optimization via Local Bayesian Optimization, called TuRBO[21]. Classical BO relies on the GP regression to built an accurate global model that is, in principle, precise enough to uncover a global optimizer. But this is really challenging in high dimensionality problem. To address these challenges, TuRBO doesn't perform a global optimization directly, but this goal is achieved by maintaining several independent local models, each involved in a separate local optimization run.

The implementation of the TuRBO algoritm was made using the Python library BoTorch[22].

Chapter 3

Results

In this final chapter, the results of the BO of the CHERAB simulation are presented. The target function chosen to minimize is the mean square error MSE. It is defined as the sum over all the pixels of the square of the difference of illuminance between the experimental and numerical result, divided by the total number of pixels.

$$MSE = \frac{\sum_{i=1}^{n.ofpixels}(illuminance_{cherab} - illuminance_{sperim})^2}{n.ofpixels} \tag{3.1}$$

Therefore, if the MSE is equal to 0, the two images are identical. Regarding the BO, an initial set of training samples is generated with a size equal to two times the number of parameters. This is done to ensure a good estimation of the posterior predictive distribution. The optimization procedure is considered finished when no better input point is found in 50 iterations. For all the CHERAB simulation, the statistical noise is taken below the 5%, in order to ensure that this doen't affect in a consistent way the results.

3.1 Shot 9229

In Figure 3.1 is illustrated the final result of the BO for the shot 9229, in comparison with the experimental results.

In general, a good qualitative agreement is achieved. The imbalance between the upper and lower limiter is manteined, with an acceptable position and values for the limiter emission. On the other hand, the maximum illuminance recorded by the simulation is lower than the experimental one. Moreover, the simulation result shows an higher elongation of the emission in the axial direction. This is mainly due to the nature of the analitical model employed, since it is difficult to correct approximate the limiter emission with a function.

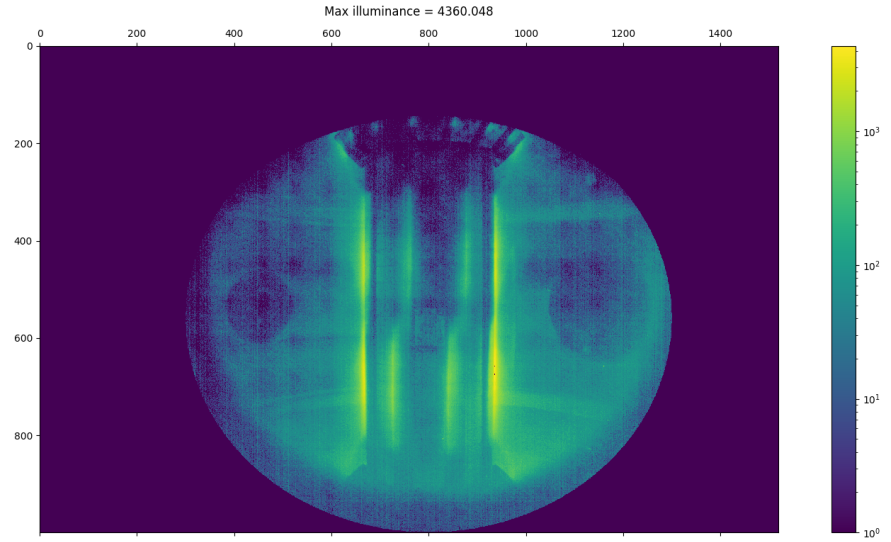

(a)

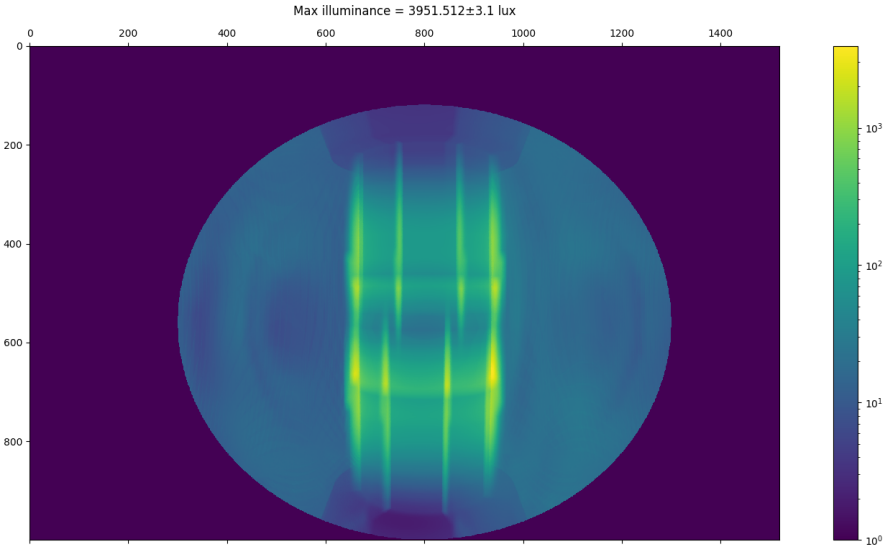

(b)

Figure 3.1: Experimental D-α view and the BO results for shot 9229.

The extracted neutral and plasma distribution are presented in the following figures. Instead, in Table 3.1 are listed the optimized values of the free parameters.

An interesting thing to notice is that the BO wasn't able to optimize the region of the passive plates. In fact, from the CHERAB simulation can be notice that seems that no emission is coming from this regions. In reality, the emission is

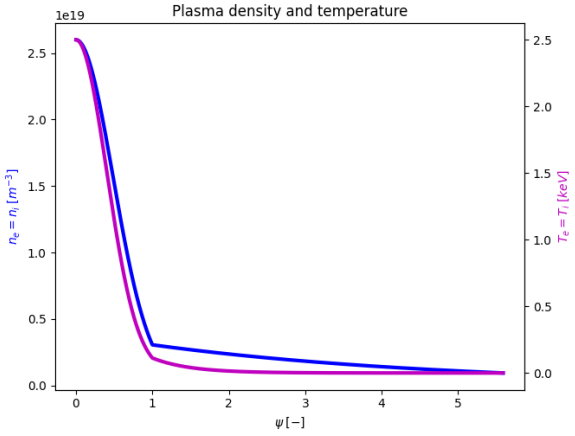

Figure 3.2: One dimensional profiles of the plasma density (blue) and temperature (purple) extracted from the final result of BO (shot 9229).

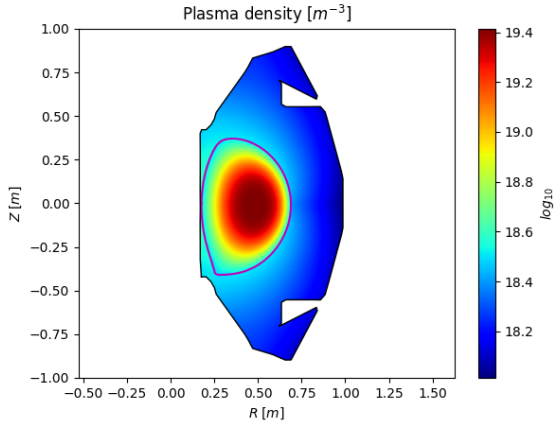

Figure 3.3: Two dimensional distribution of the plasma density extracted from the final result of BO (shot 9229).

present, but the BO found really smaller values for the Guassian parameters and, as result, their contributions is not captured. This can be due to the fact that the MSE represent an integral value, and it is possible that the overall contribution to the minimization of the function is not so important. For what regards the plasma distribution, the profiles are quite similar to the ones find "manually" in [11], with the exception of the plasma density. It exhibits a sharper decrease in the core, while in the edge the exponential decay is much slower.

In Figure 3.7 is shown the convergence of the target function. As can be

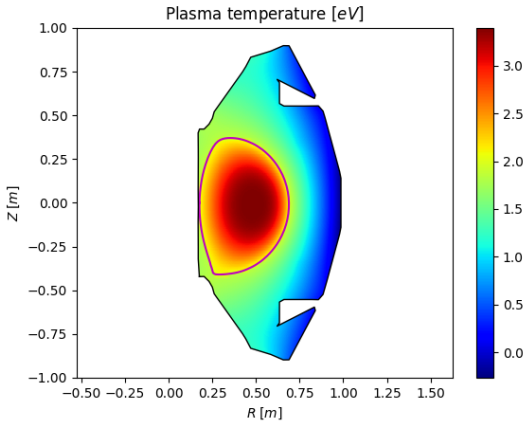

Figure 3.4: Two dimensional distribution of the plasma temperature extracted from the final result of BO (shot 9229).

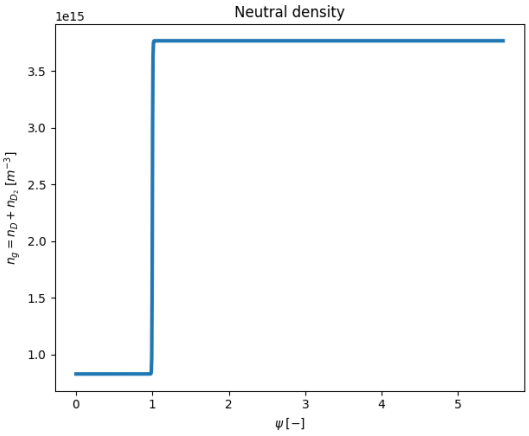

Figure 3.5: One dimensional reproduction of the background neutral density extracted from the final result of BO (shot 9229).

appreciated, the search space is really huge and the MSE can acquire really high value. Nevertheless, it is not possible to reduce a priori the search space, but can be possible to run successive BO in order to reduce the dimensionality of the problem.

Instead in Figure 3.8 is shown the convergence of two different parameters, respecticily the radial position of the limiter Gaussian and neutral density in the core. As can be appreciated, the parameter search is gradually reduced when the posterior predictive distribution acquire enough information to correctly model the target function.

An important consideration regards the parametric study proposed in [11]. As

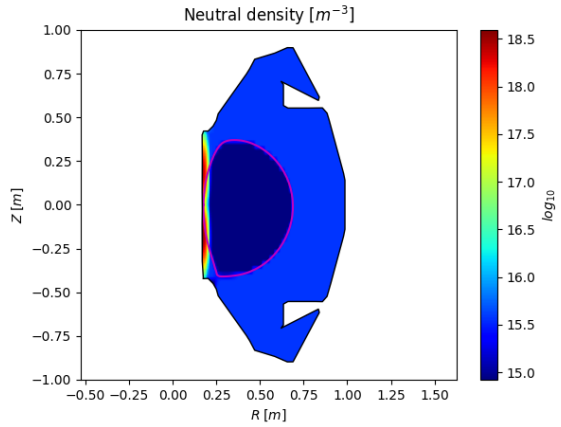

Figure 3.6: Two dimensional distribution of the neutral density extracted from the final result of BO (shot 9229).

$n_g^{\psi_N=0}$	$8.3 \cdot 10^{14}\,\mathrm{m}^{-3}$	$n_g^{\psi_N\to\infty}$	$3.7 \cdot 10^{15}\,\mathrm{m}^{-3}$
μ_g	$2.8 \cdot 10^{-3}$	$\sigma_{g,R}$	$2.1 \cdot 10^{-4}$
$\sigma_{g,Z}$	$1.0 \cdot 10^{-2}$	$n_{g,0}^{R,upper}$	$3.2 \cdot 10^{18}\,\mathrm{m}^{-3}$
$n_{g,0}^{R,lower}$	$4.1 \cdot 10^{18}\,\mathrm{m}^{-3}$	R_s	$0.17\,\mathrm{m}$
Z_s^{upper}	$0.18\,\mathrm{m}$	Z_s^{lower}	$-0.18\,\mathrm{m}$
$n_{g,0}^{div,upper}$	$8.6 \cdot 10^{18}\,\mathrm{m}^{-3}$	$n_{g,0}^{div,lower}$	$3.0 \cdot 10^{18}\,\mathrm{m}^{-3}$
R_{div}	$0.21\,\mathrm{m}$	Z_{div}^{upper}	$0.42\,\mathrm{m}$
Z_{div}^{lower}	$-0.49\,\mathrm{m}$	$\sigma_{g,R}^{div}$	$1.2 \cdot 10^{-4}$
$\sigma_{g,Z}^{div}$	$1.3 \cdot 10^{-5}$	$n_e^{\psi_N=1}$	$3.1 \cdot 10^{18}\,\mathrm{m}^{-3}$
$\lambda_n^{\psi_N}$	3.88	$T_e^{\psi_N=1}$	112 eV
$\lambda_T^{\psi_N}$	0.49	c_{upper}	0.057
c_{lower}	0.121	$c_{smoothing}$	0.1

Table 3.1: Final values of the free parameters after the BO for the shot 9229.

shown, not all the parameters have the same influence on the CHERAB result. Nevertheless, the BO shows that also the parameter that have pratically no influence on the MSE tends to converge, like the neutral density in the core. Anyway, the results for these parameters must be treated carefully.

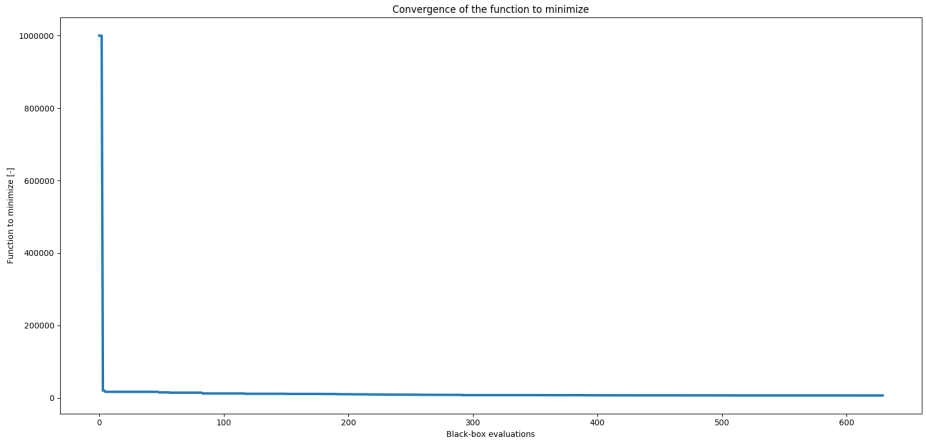

(a)

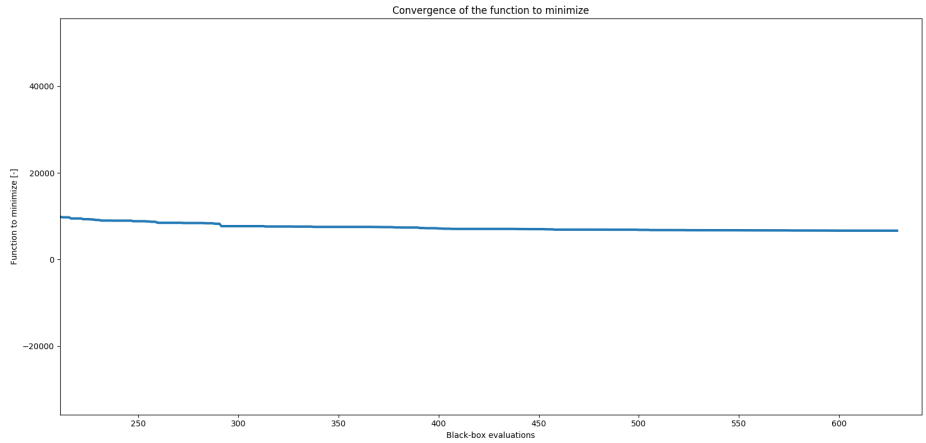

(b)

Figure 3.7: Convergence of the MSE function with a zoom in the last iterations (b) for shot 9229.

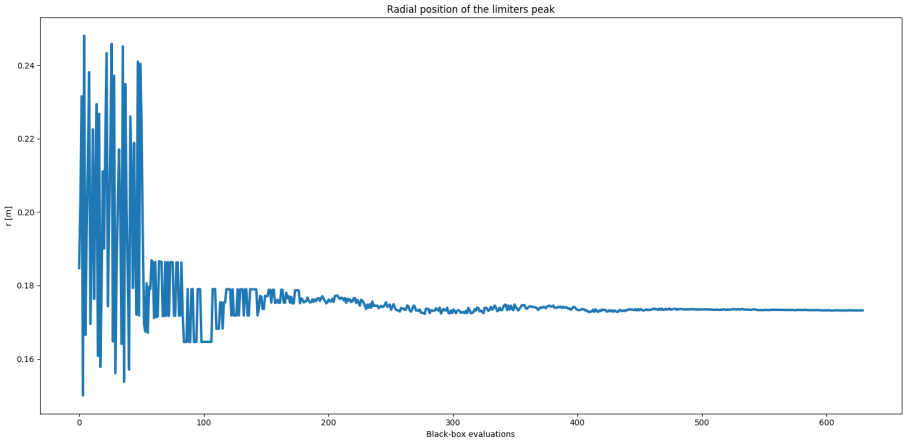

(a)

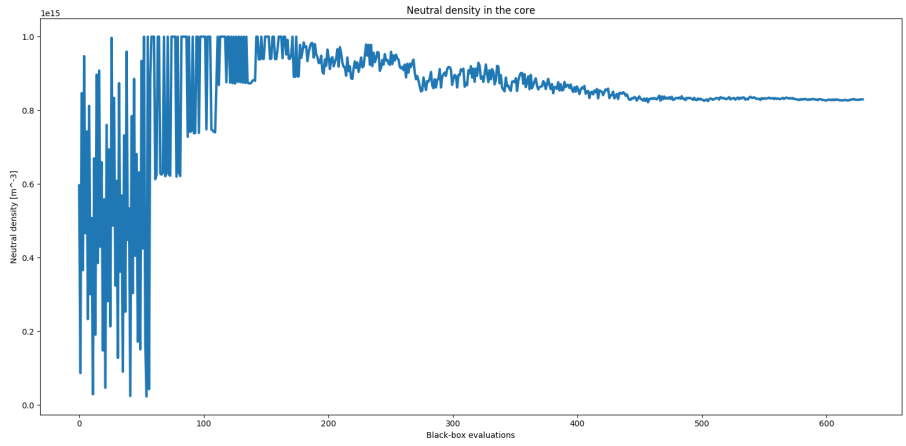

(b)

Figure 3.8: Convergence of the radial position of the limiter Gaussian (a) and the neutral density in the core (b) (shot 9229).

3.2 Shot 10041

In Figure 3.9 is illustrated the final result of the BO for the shot 10041, in comparison with the experimental results.

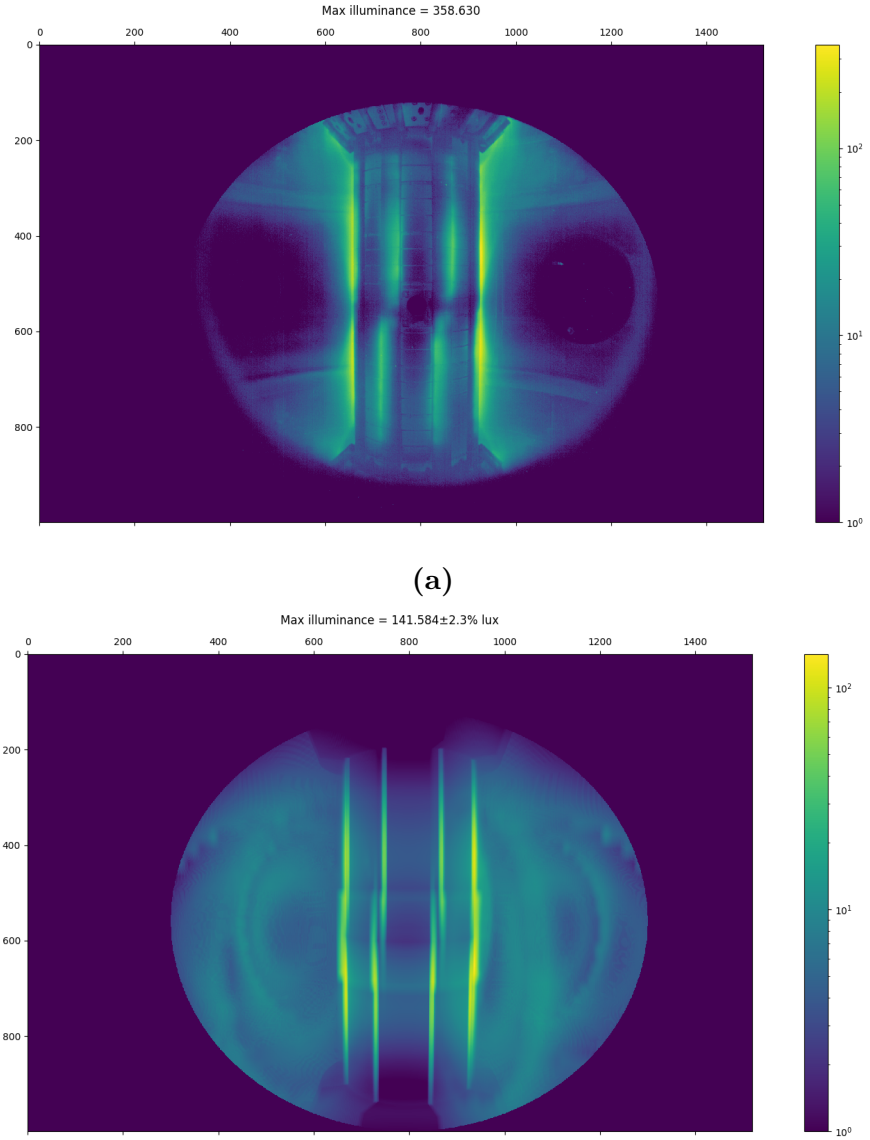

(a)

(b)

Figure 3.9: Experimental D-α view and the BO results for shot 10041.

The same general comment made for the shot 9229 are applicable for this case. A good qualitative agreement is reached, an imbalance between the upper and

lower limiter is kept. Anyway, the maximum illuminance not correspond to the experimental one. In this case, the difference is actually more accentuated. The same is true for the elongation of the emission in the axial direction.

The extracted neutral and plasma distribution are presented in the following figures. Instead, in Table 3.2 are listed the optimized values of the free parameters.

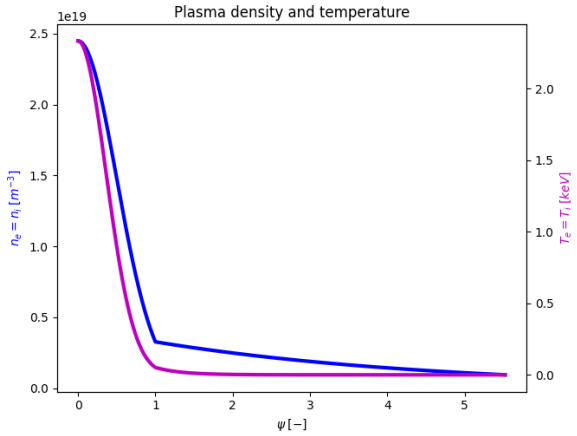

Figure 3.10: One dimensional profiles of the plasma density (blue) and temperature (purple) extracted from the final result of BO (shot 10041).

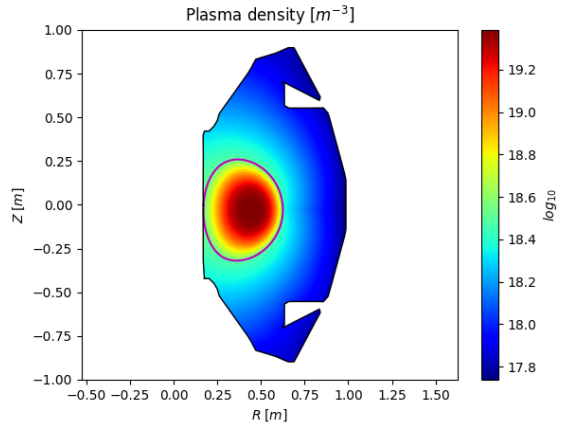

Figure 3.11: Two dimensional distribution of the plasma density extracted from the final result of BO (shot 10041).

Also in this case, the BO doesn't optimize the region of the passive plates. The plasma temperature and density shown the same profile of the previuos case. The only difference is that with the magnetic configuration so compressed, the

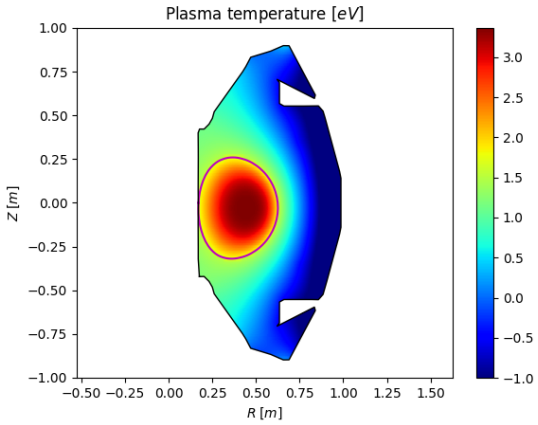

Figure 3.12: Two dimensional distribution of the plasma temperature extracted from the final result of BO (shot 10041).

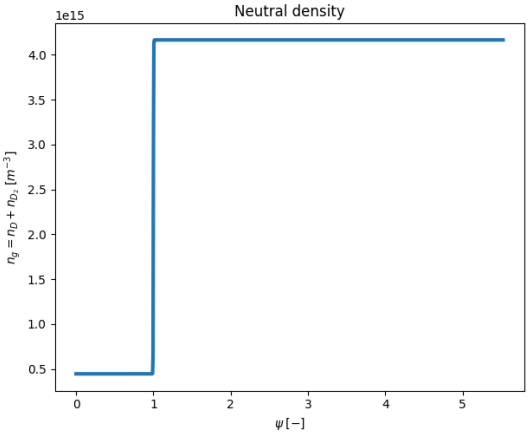

Figure 3.13: One dimensional reproduction of the background neutral density extracted from the final result of BO (shot 10041).

elongation in the axial direction is emphasized.

In Figure 3.15 is shown the convergence of the target function. Respect to the shot 9229, the convergence requirement is met much before. This can be due to the lower experimental illuminance.

Instead in Figure 3.16 is shown the convergence of the radial position of the limiter Gaussian and neutral density in the core. In this case, the parameters convergence is much worst with respect to the shot 9229.

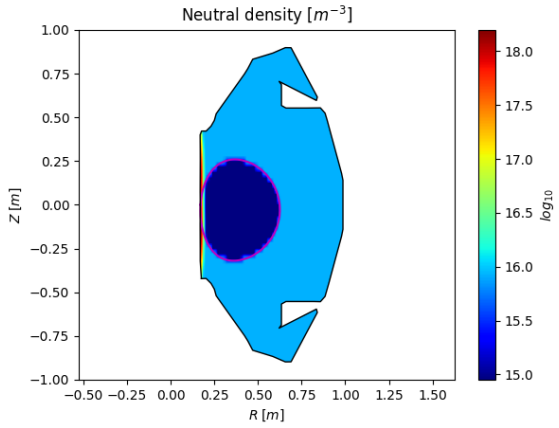

Figure 3.14: Two dimensional distribution of the neutral density extracted from the final result of BO (shot 10041).

$n_g^{\psi_N=0}$	$4.1 \cdot 10^{14}\,\mathrm{m}^{-3}$	$n_g^{\psi_N\to\infty}$	$4.4 \cdot 10^{15}\,\mathrm{m}^{-3}$
μ_g	$1.5 \cdot 10^{-3}$	$\sigma_{g,R}$	$2.1 \cdot 10^{-4}$
$\sigma_{g,Z}$	$2.0 \cdot 10^{-2}$	$n_{g,0}^{R,upper}$	$6.4 \cdot 10^{18}\,\mathrm{m}^{-3}$
$n_{g,0}^{R,lower}$	$8.2 \cdot 10^{18}\,\mathrm{m}^{-3}$	R_s	$0.15\,\mathrm{m}$
Z_s^{upper}	$0.15\,\mathrm{m}$	Z_s^{lower}	$-0.14\,\mathrm{m}$
$n_{g,0}^{div,upper}$	$1.1 \cdot 10^{18}\,\mathrm{m}^{-3}$	$n_{g,0}^{div,lower}$	$1.3 \cdot 10^{18}\,\mathrm{m}^{-3}$
R_{div}	$0.23\,\mathrm{m}$	Z_{div}^{upper}	$0.46\,\mathrm{m}$
Z_{div}^{lower}	$-0.47\,\mathrm{m}$	$\sigma_{g,R}^{div}$	$1.1 \cdot 10^{-4}$
$\sigma_{g,Z}^{div}$	$1.5 \cdot 10^{-5}$	$n_e^{\psi_N=1}$	$3.3 \cdot 10^{18}\,\mathrm{m}^{-3}$
$\lambda_n^{\psi_N}$	3.63	$T_e^{\psi_N=1}$	51 eV
$\lambda_T^{\psi_N}$	0.33	c_{upper}	0.061
c_{lower}	0.105	$c_{smoothing}$	0.045
$n_e^{\psi_N=0}$	$2.5 \cdot 10^{18}\,\mathrm{m}^{-3}$	$T_e^{\psi_N=0}$	2333 eV

Table 3.2: Final values of the free parameters after the BO for the shot 10041.

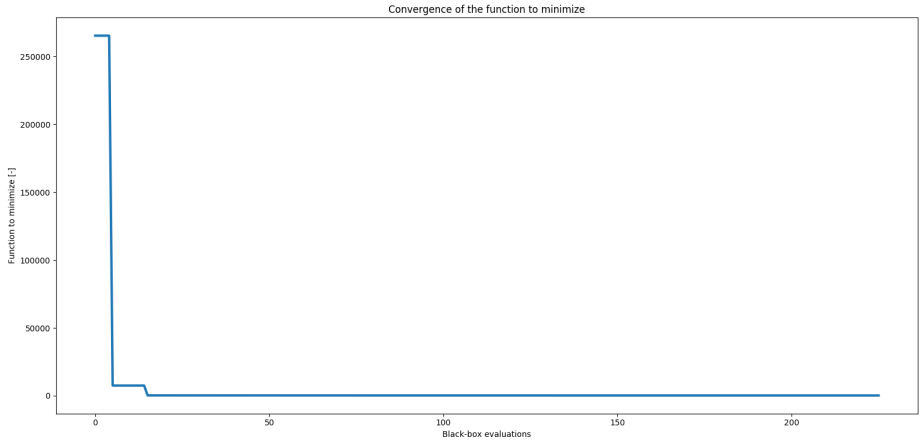

(a)

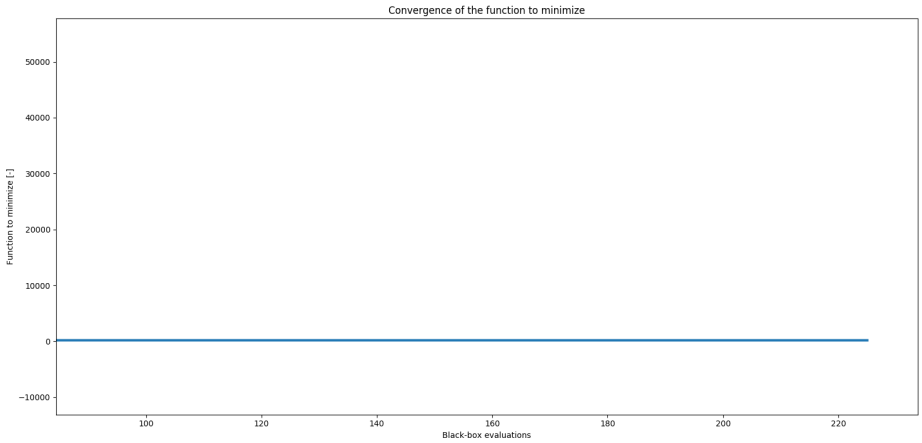

(b)

Figure 3.15: Convergence of the MSE function with a zoom in the last iterations (b) for the shot 10041.

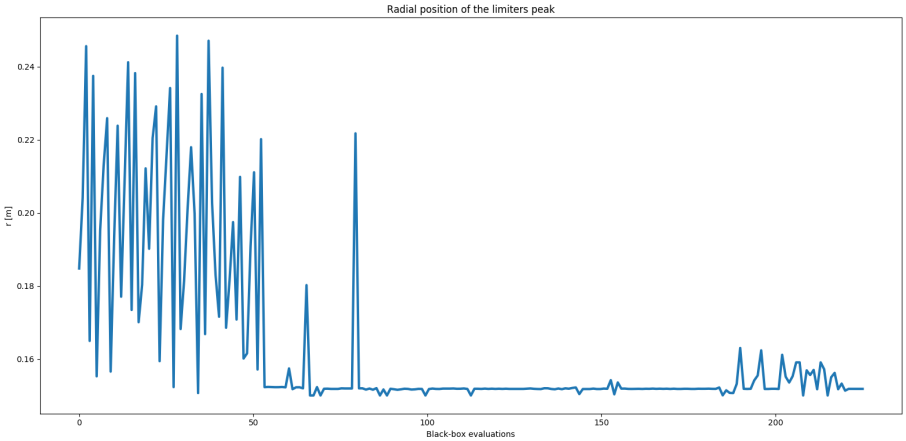

(a)

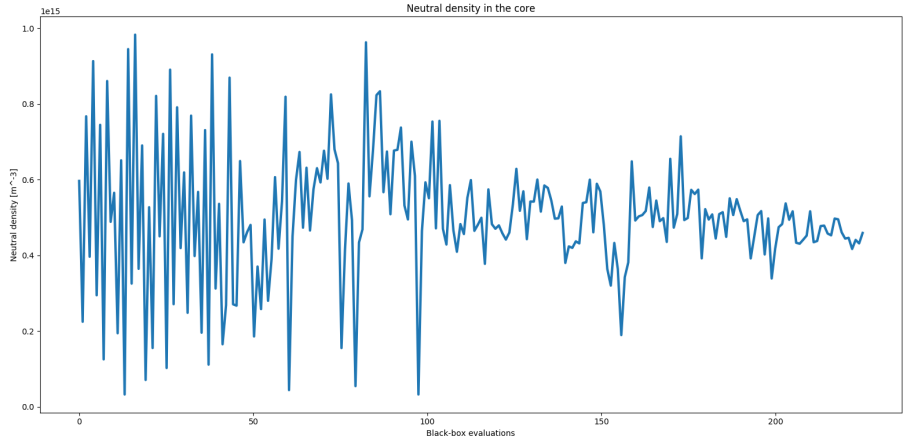

(b)

Figure 3.16: Convergence of the radial position of the limiter Gaussian (a) and the neutral density in the core (b) (shot 10041).

Chapter 4

Conclusion

Synthetic diagnostics are becoming a flexible and accurate solution for analyse experimental data in the nuclear fusion community. Of particular interest is the D-α camera, from which it possible to infer the distribution of neutrals inside the plasma chamber.

In this work, Bayesian optimization algoritm has been applied to the CHERAB code in order to reproduce the experimental result of the D-α camera for two plasma shot in the ST40 tokamak. Starting from an analitical model for the plasma and neutral distributions, the CHERAB code is able to compute the 2D perspective of a synthetic D-α camera. Unfortunatly, the analitical models rely on numerous free parameters, that must be weel chosen in order to have an agreement with the experimental data and actually infer the neutral distribution. To set these parameters, Bayesian optimization algoritm has been used. In particular, since the dimensionality of the problem is really high, the Scalable Global Optimization via Local Bayesian Optimization (TuRBO) has been employed. The results obtained for both shots reveal a remarkable qualitative agreement. Nevertheless, a good quantitative agreement is not reached. This is due mainly to intrinsic three-dimensionality of the ST40 emission and to the inadequacy of the analitical models to catch these complicated features. Anyway, constructing D-α emission source from sophisticated code, such as SOLPS-ITER, is computationally really expensive. Therefore, the setup presented remain a valuable alternative if there is the necessity of having a fast and meaningful analysis.

Bibliography

[1] David Moiraf. *The use of Plasma Mirror for Relativistic Electron Generation Relevant to Fast Ignition in Inertial Confinement Fusion*. PhD thesis, July 2020 (cit. on p. 2).

[2] URL: https://www.euro-fusion.org/programme/demo/ (cit. on p. 3).

[3] T Klinger et al. «Performance and properties of the first plasmas of Wendelstein 7-X». In: *Plasma Physics and Controlled Fusion* 59.1 (Oct. 2016), p. 014018. DOI: 10.1088/0741-3335/59/1/014018. URL: https://dx.doi.org/10.1088/0741-3335/59/1/014018 (cit. on p. 3).

[4] Alexander P J van Deursen, David Beltran, and P.C.T. van der Laan. «Grounding and cabling aspects inside the ITER cryostat». In: *2014 XXXIth URSI General Assembly and Scientific Symposium (URSI GASS)* (2014), pp. 1–4. URL: https://api.semanticscholar.org/CorpusID:36333372 (cit. on p. 4).

[5] URL: www.fusion.org.uk (cit. on p. 6).

[6] G F Counsell, R Martin, T Pinfold, D Taylor, and the MAST team. «On the magnitude and distribution of halo currents during disruptions on MAST». In: *Plasma Physics and Controlled Fusion* 49.4 (Mar. 2007), p. 435. DOI: 10.1088/0741-3335/49/4/007. URL: https://dx.doi.org/10.1088/0741-3335/49/4/007 (cit. on p. 7).

[7] A. Sykes et al. «First results from MAST». In: *Nuclear Fusion* 41.10 (Oct. 2001), p. 1423. DOI: 10.1088/0029-5515/41/10/310. URL: https://dx.doi.org/10.1088/0029-5515/41/10/310 (cit. on p. 8).

[8] M. Gryaznevich, TE. Ltd Physics Team, and TE. Ltd HTS Team for Tokamak Energy Ltd. «Experiments on ST40 at high magnetic field». In: *Nuclear Fusion* 62.4 (Feb. 2022), p. 042008. DOI: 10.1088/1741-4326/ac26ee. URL: https://dx.doi.org/10.1088/1741-4326/ac26ee (cit. on p. 8).

[9] S.A.M. McNamara et al. «Achievement of ion temperatures in excess of 100 million degrees Kelvin in the compact high-field spherical tokamak ST40». In: *Nuclear Fusion* 63.5 (Mar. 2023), p. 054002. DOI: 10.1088/1741-4326/acbec8. URL: https://dx.doi.org/10.1088/1741-4326/acbec8 (cit. on p. 8).

[10] Matthew Carr, Jack Lovell, Matej Tomes, Vlad Neverov, Dr Alex Meakins, Koyo MUNECHIKA, Dominik Stańczak, and David Bold. *cherab/core: Release v1.3.0*. Version v1.3.0. Dec. 2021. DOI: 10.5281/zenodo.5778961. URL: https://doi.org/10.5281/zenodo.5778961 (cit. on pp. 9, 12).

[11] A. Aimetta et al. «Forward modelling of Dα camera view in ST40 informed by experimental data». In: *Fusion Engineering and Design* 190 (2023), p. 113513. ISSN: 0920-3796. DOI: https://doi.org/10.1016/j.fusengdes.2023.113513. URL: https://www.sciencedirect.com/science/article/pii/S0920379623000972 (cit. on pp. 9, 14, 18, 31, 32).

[12] P.C. Stangeby. *The Plasma Boundary of Magnetic Fusion Devices (1st ed.)* CRC Press., 2000. DOI: https://doi.org/10.1201/9780367801489 (cit. on pp. 10, 11, 14, 15).

[13] Dr Alex Meakins and Dr Matthew Carr. *Raysect Python Raytracing Package*. Version v0.4.0. Mar. 2018. DOI: 10.5281/zenodo.1205064. URL: https://doi.org/10.5281/zenodo.1205064 (cit. on p. 12).

[14] Jeffrey P. Freidberg. In: *Plasma Physics and Fusion Energy*. Cambridge University Press, 2007 (cit. on p. 13).

[15] Detlev Reiter. «The data file AMJUEL: Additional atomic and molecular data for EIRENE». In: (Jan. 2000) (cit. on p. 14).

[16] L.L. Lao, H. St. John, R.D. Stambaugh, A.G. Kellman, and W. Pfeiffer. «Reconstruction of current profile parameters and plasma shapes in tokamaks». In: *Nuclear Fusion* 25.11 (Nov. 1985), p. 1611. DOI: 10.1088/0029-5515/25/11/007. URL: https://dx.doi.org/10.1088/0029-5515/25/11/007 (cit. on p. 14).

[17] W. L. Wiese and J. R. Fuhr. «Accurate Atomic Transition Probabilities for Hydrogen, Helium, and Lithium». In: *Journal of Physical and Chemical Reference Data* 38.3 (June 2009), pp. 565–720. ISSN: 0047-2689. DOI: 10.1063/1.3077727. eprint: https://pubs.aip.org/aip/jpr/article-pdf/38/3/565/15667142/565_1_online.pdf. URL: https://doi.org/10.1063/1.3077727 (cit. on p. 18).

[18] Jurgen R. Meyer-Arendt. «Radiometry and Photometry: Units and Conversion Factors». In: *Appl. Opt.* 7.10 (Oct. 1968), pp. 2081–2084. DOI: 10.1364/AO.7.002081. URL: https://opg.optica.org/ao/abstract.cfm?URI=ao-7-10-2081 (cit. on p. 18).

[19] Peter I. Frazier. *A Tutorial on Bayesian Optimization*. 2018. arXiv: 1807.02811 [stat.ML] (cit. on pp. 21, 28).

[20] Carl Edward Rasmussen and Christopher K. I. Williams. *Gaussian Processes for Machine Learning*. The MIT Press, Nov. 2005. ISBN: 9780262256834. DOI: 10.7551/mitpress/3206.001.0001. URL: https://doi.org/10.7551/mitpress/3206.001.0001 (cit. on p. 22).

[21] David Eriksson, Michael Pearce, Jacob Gardner, Ryan D Turner, and Matthias Poloczek. «Scalable Global Optimization via Local Bayesian Optimization». In: *Advances in Neural Information Processing Systems*. 2019, pp. 5496–5507. URL: http://papers.nips.cc/paper/8788-scalable-global-optimization-via-local-bayesian-optimization.pdf (cit. on p. 28).

[22] Maximilian Balandat, Brian Karrer, Daniel R. Jiang, Samuel Daulton, Benjamin Letham, Andrew Gordon Wilson, and Eytan Bakshy. «BoTorch: A Framework for Efficient Monte-Carlo Bayesian Optimization». In: *Advances in Neural Information Processing Systems 33*. 2020. URL: https://proceedings.neurips.cc/paper/2020/hash/f5b1b89d98b7286673128a5fb112cb9a-Abstract.html (cit. on p. 28).